THE 158 MICRON [C II] LINE: A MEASURE OF GLOBAL STAR FORMATION ACTIVITY IN GALAXIES

G. J. STACEY,[1] N. GEIS,[2] R. GENZEL,[2] J. B. LUGTEN,[3] A. POGLITSCH,[2] A. STERNBERG,[2] AND C. H. TOWNES[1]
Received 1990 July 5; accepted 1990 November 20

ABSTRACT

We report 55″ resolution KAO observations of the 158 μm [C II] fine-structure line emission from a sample of 14 gas-rich galaxies. Of this sample, five were studied with a new spatial array which gives a simultaneous three-point measurement. Fully sampled velocity channel maps at 125 km s^{-1} resolution were obtained for the central 2 kpc of the archetypical starburst galaxy, M82. The galaxies sampled include a wide variety of spectral types from the early RSab galaxy NGC 4736 to the late Scd spiral galaxy NGC 6946 and span a range of far-infrared luminosity classes from the lower luminosity Sc NGC 5907 to the ultraluminous *IRAS* galaxies NGC 3690 and NGC 6240. ($L_{\rm FIR} \approx 5 \times 10^{11}$ $L_{\odot}$). Our results are combined and analyzed together with a previous sample of six infrared bright galaxies, observations of the LMC 30 Doradus region, and a sample of Galactic sources.

The [C II] line is an important cooling line in galaxies, accounting for 0.1%-1% of the far-infrared luminosity of the nuclear regions. The brightness of the [C II] line indicates that it is produced in the warm ($T_{\rm gas} > 200$ K), dense ($n_{\rm H} > 10^3$ cm^{-3}) photodissociated gas at the interface regions between giant molecular clouds and fully ionized media. The photodissociated gas may represent a substantial fraction (up to $\approx 40\%$) of the total gas mass in starburst nuclei. Much of the observed 21 cm line emission from starburst nuclei may originate in these dense photodissociation regions, lending support to the contention that much of the atomic gas in galaxies may result from the photodissociation of molecular clouds by nearby OB stars. The [C II] line is correlated with the FIR continuum intensity and is therefore a measure of the excitation of the neutral interstellar medium by the average external UV radiation field.

The [C II] to ^{12}CO (1 → 0) line intensity ratio is a diagnostic of global star formation activity in galaxies. The ratio obtained for starburst nuclei is constant and equals the ratio measured for Galactic star-forming regions. This implies that, as in Galactic star-forming regions, the excitation temperature of the ^{12}CO (1 → 0) transition in the molecular clouds in starburst nuclei is substantially higher than in Galactic disk molecular clouds. The ^{12}CO (1 → 0) line may, therefore, *not* be a reliable tracer of molecular mass in starburst nuclei. The observed intensities of the [C II] line in starburst nuclei indicate that the bulk of the molecular media in these regions is exposed to UV fields which are more than 1000 times the intensity of the average UV field in the solar neighborhood. The [C II]/^{12}CO (1 → 0) line intensity ratio in *nonstarburst nuclei* is a factor of 3 smaller than the value observed for starburst nuclei—similar to the ratio found for Galactic giant molecular clouds. This suggests that in nonstarburst galaxies the ^{12}CO (1 → 0) emission is not severely affected by external UV radiation fields. The ultraluminous *IRAS* galaxy NGC 6240 has a small [C II]/^{12}CO (1 → 0) line intensity ratio which implies that this galaxy is *not* currently undergoing a global burst of star formation activity.

Subject headings: galaxies: interstellar matter — galaxies: structure — infrared: spectra

1. INTRODUCTION

Recent observations of the far-infrared (FIR) fine-structure lines of singly ionized carbon, singly ionized silicon, and neutral oxygen demonstrate that a wealth of information on the physical conditions of the warm neutral interstellar medium may be obtained from the study of their integrated line intensities and profiles. The brightest of these lines, the $^3P_1 \rightarrow {}^3P_2$ (63.1837 μm) transition of O^0 and the $^2P_{3/2} \rightarrow {}^2P_{1/2}$ (157.7409 μm) transition of C$^+$ have proven to be useful for the study of a wide variety of Galactic regions including planetary nebulae, H II regions, surfaces of molecular clouds, and in

general cuts across the Galactic plane (cf. Genzel, Harris, & Stutzki 1989; Genzel & Stacey 1985, and references therein). The observations reveal that between a few and several tens of percent (depending on the star formation activity) of the neutral interstellar medium is contained in warm, dense photodissociation regions (PDRs) found at the interfaces between fully ionized and neutral interstellar gas clouds. At these interfaces, far-ultraviolet radiation longward of the Lyman limit (912 → 2000 Å) escapes the H II regions, penetrates into the molecular cloud where it heats the neutral gas, dissociates most molecules, and ionizes atoms with ionization potentials less than 13.6 eV. Photodissociation regions are widespread. The penetration depth of far-UV radiation into molecular clouds is larger than the penetration depth of Lyman-continuum radiation into H II regions, and is limited by dust extinction to $A_V < 5$ (Werner 1970; Walmsey 1975; Langer 1976). Furthermore, widespread far-UV radiation in galaxies is produced by the numerous B stars which do not contribute

[1] Department of Physics, University of California, Berkeley, CA 94720.
[2] Max-Planck-Institut für Physik und Astrophysik, Institut für extra-terrestrische Physik, D-8046 Garching bei München, Federal Republic of Germany.
[3] Radio Astronomy Laboratory, 601 Campbell Hall, University of California, Berkeley, CA 94720.

significantly to the Lyman-continuum flux. Photodissociation regions are warm ($T_{gas} \sim 100$–1000 K) and are probably heated by photoelectric emission from grain surfaces and large molecules in low-density regions, and by the collisional deexcitation of UV pumped vibrationally excited H_2 in high-density regions. The gas is cooled by the FIR fine-structure line radiation of O^0, Si^+, and C^+, and in high-density regions by molecular rotational emission and gas-grain collisions as well (Tielens & Hollenbach 1985; Sternberg & Dalgarno 1989).

Measurements of the [C II] line in external galaxies were previously reported by Crawford et al. (1985, hereafter CGTW) who studied the 158 μm line in six nearby infrared-bright galaxies. They related their measurements to the $J = 1 \rightarrow 0$ line of ^{12}CO, the FIR continuum and the 21 cm line emission in these galaxies and found (1) the [C II] line is bright, amounting to typically 0.5% of the bolometric luminosity of these galaxies; (2) [C II] and ^{12}CO $(1 \rightarrow 0)$ integrated line intensities and spatial distribution are well correlated; (3) [C II] line emission is not correlated with 21 cm atomic hydrogen emission; and (4) [C II] radiation is well correlated with far-infrared (FIR) continuum radiation (which is a measure of the far-UV energy density). Points (2) and (3) indicate that the [C II] line radiation is associated with molecular clouds—not with atomic gas clouds or the intercloud medium. Point (4) indicates that the [C II] line intensity traces the local UV field strength. Together with point (2), this indicates that at least in IR-bright galactic nuclei, the ^{12}CO $(1 \rightarrow 0)$ line emission may also be heavily affected by the local UV fields and thus not reliably trace molecular mass.

We have extended the CGTW study to include both a wider range of luminosity classes in IR-bright galaxies and to include a wide spectral range of spiral galaxies not noted for excessive star formation. The sample includes 13 new galaxies of which 11 were detected in [C II] and four were mapped. New fully sampled channel maps of the inner 1.9 kpc regions of the archetypical starburst galaxy, M82, are also presented in addition to 7.3 kpc strip map scans of the [C II] radiation along the major and minor axis of this galaxy.

2. OBSERVATIONS

2.1. Spectral Scans

We made our observations using three versions of the U. C. Berkeley cryogenic tandem Fabry-Perot spectrometer on the 91.4 cm telescope on board the Kuiper Airborne Observatory (KAO). The data were taken over 4 years during 12 separate flights spanning eight flight series. The galaxies and observational parameters are summarized in Table 1. The spectral resolution used was chosen individually for each galaxy depending on the expected line flux and velocity width. The sensitivity of each observation depended on both the version of the instrument used and on the spectral resolution employed [at a fixed wavelength, λ, the noise equivalent power (NEP) α $(\Delta\lambda/\lambda)^{1/2}$]. The data for NGC 6946 were taken with the original version of the spectrometer (Storey, Watson, & Townes 1980; Watson 1982) using a single stressed Ge : Ga photoconductor (Haller, Hueschen, & Richards 1979) and warm scanning Fabry-Perot etalons. The spectrometer was used at a spectral resolution of 80 km s^{-1} and the system NEP including all telescope and instrument loses was 8×10^{-15} W Hz$^{-1/2}$. Data taken between 1985 February and 1987 January were taken with an improved version of the spectrometer (Lugten 1987) which incorporated both high resolution optics and scanning stage and improved fixed Fabry-Perot filters. Cooling the second scanning Fabry-Perot etalon to 78 K decreased the NEP to about 5–7×10^{-15} W Hz$^{-1/2}$. Measurements during 1988 were taken with the latest version of the tandem Fabry-Perot which incorporates a three-element detector array (see below). The three elements allow one to map simultaneously three spatial positions on the source. The on-axis (central) detector for these observations typically achieves a system NEP at 100 km s^{-1} resolution of about 4×10^{-15} W Hz$^{-1/2}$. For all of the observations reported, our beam size was 55″ (FWHM) with a total solid angle of 8.6×10^{-8} sr (68″ equivalent disk). Line flux calibration (accuracy $\pm 30\%$) was determined through comparison with the known continuum levels of astronomical sources measured on the same flight (Table 1,

TABLE 1

OBSERVING LOG FOR PROGRAM GALAXIES

Galaxy (1)	R.A. (1950) (2)	Decl. (1950) (3)	Type[a] (4)	Velocity Resolution (km s^{-1}) (5)	Observation Date (6)	Calibration[b] (7)
NGC 660	01^{h}40^{m}20^{s}7	13°23′32″	SB(s)a pec	155	1986 Nov 4	Hot load
NGC 891	02 19 24.5	42 07 13	SA(s)b	200	1986 Jul 29	Jupiter
Maffei II	02 38 10.1	59 23 32	SAB(rs)bc	120	1986 Jul 26	Jupiter
NGC 2146	06 10 40.1	78 22 23	SB(s)ab pec	125	1988 Jan 13	Jupiter
M82	09 51 43.9	69 55 01	IO	125	1988 Jan 20	Jupiter
NGC 3079	09 58 35.0	55 55 17	SB(s)c	125	1988 Jan 15	Jupiter
NGC 3109	10 00 49.0	−25 55 00	SB(s)m	230	1986 May 1	Saturn
NGC 3628	11 17 39.6	13 51 48	Sb pec	100	1988 Jun 15	W49 NW
NGC 3690/IC 694	11 25 44.2	58 50 18	IBm pec	195	1985 Feb 26	BN-KL
NGC 4565	12 33 52.2	26 15 34	SA(s)b	140	1987 Jun 6	Moon
NGC 4736	12 48 32.0	41 23 36	RSA(r)ab	100	1988 Jun 15	W49 NW
NGC 5907	15 14 36.8	56 30 23	SA(s)c	125	1988 Jun 17	Hot load
NGC 6240	16 50 28.0	02 29 00	IO pec	200	1986 Jul 29	Jupiter
				125	1988 Jun 15	W49 NW
NGC 6946	20 33 48.8	59 58 50	SAB(rs)cd	80	1984 Jul 29	W49 NW

[a] Galaxy classifications are from de Vaucouleurs, de Vaucouleurs, & Corwin 1976.

[b] Calibrated with respect to the Moon and planets, we find $S_\nu(158~\mu m) = 17,600$ and $42,000$ Jy in our 55″ beam for W49 NW and BN-KL respectively. The "hot load" denotes our internal blackbody which has been calibrated numerous times with respect to the planets. At 158 μm, our blackbody emits 9.8×10^5 Jy.

col. [7]). Radial velocities of the [C II] $^2P_{3/2} \rightarrow {}^2P_{1/2}$ line (rest wavelength 157.7409 μm; Cooksy, Blake, & Saykally 1986) were determined for the various galaxies relative to absorption cell measurements of H_2S at 157.7726 and 159.5189 μm (Flaud, Camy-Peyret, & Johns 1983), D_2O at 158.4669 and 161.3446 μm, HDO at 161.7115 μm, and $H_2^{18}O$ at 158.2584 μm (Johns 1985). Changes in the Fabry-Perot spacing during a scan were measured and servocontrolled with a Hewlett-Packard Zeeman-split laser interferometer. The velocity scales thus determined are accurate to ± 10 to 20 km s^{-1} depending on the velocity resolution employed. The chopper throw was typically 3'–4' at 33 Hz perpendicular to the major axis of the galaxies. Absolute pointing was accurate to $\pm 20''$ and relative pointing during a typical integration (~ 30–45 minutes) was better than 10''.

2.2. Raster Scan Mapping of M82

In 1988 January, we used our three-channel system to construct raster scan maps of the inner 120'' regions of M82 and strip maps of 7.33 extent along both the major and minor axis in [C II]. The maps were centered on the 2 μm peak: R.A. = $09^h51^m43.9$, decl. = $69°55'01.0$ (1950) (Rieke et al. 1980). The raster maps of the inner regions were obtained by fixing the Fabry-Perot etalon spacing for the desired velocity and then raster-scanning the telescope beam over the source. The velocity resolution was 125 km s^{-1}, and typical integration time per point was 20 s. Three-channel maps at center velocities of 90, 190, and 295 km s^{-1} were constructed. Each map was sampled every 30'' by the central detector. The side channels were at a position angle of 117° during these observations and thus sampled the C II emission from regions ($+49''$, $-25''$) and ($-49''$, $+25''$) in right ascension and declination with respect to the central channel. The side channels were used to increase the signal-to-noise ratio in the central regions of the map, to increase the map sampling, and to extend the map borders. The strip maps were constructed by sampling every 40'' along the major and minor axis for a total scan of 3.67 on both sides of the galactic nucleus. We made channel strip maps along the major axis at the three velocity centers indicated above. Along the minor axis we measured only at the central velocity (190 km s^{-1}).

2.3. Millimeter Wave Spectroscopy

For many of the galaxies we studied, CO ($J = 1 \rightarrow 0$) spectra (taken with beams of similar size) are available in the literature. For those sources with no such published spectra (NGC 4565 and NGC 5907), and for the off axis channels in the galaxies NGC 3079 and NGC 4736, we obtained ^{12}CO spectra with the NRAO 12 m telescope on Kitt Peak.[4] The data were obtained on 1988 July 8 and 9, using an SIS mixer receiver ($T_{ssb} \sim 170$ K) and a 512 MHz bandwidth spectrometer with 2 MHz velocity resolution. The data were typically binned to 20 km s^{-1} resolution. The beam size at the 12 m telescope is 55'' FWHM, identical to our KAO beam size. The data were calibrated using an ambient temperature chopper wheel and scaled to the ^{12}CO (1 $\rightarrow$ 0) emission from the Orion Nebula for which we assume $T_R^* = 75$ K (P. Jewel, personal communication).

3. THREE-ELEMENT STRESSED DETECTOR ARRAYS

3.1. Design

To achieve spatial multiplexing, we installed a stack of three stressed Ge : Ga photoconductive detectors in our Fabry-Perot spectrometer. For maximum mapping efficiency (and to minimize the effects of walkoff and beam divergence in the Fabry-Perot; see below), it is desirable to have the side channels as close as possible to the central detector. The spectrometer's plate scale at the detector is 45'', or approximately one diffraction-limited beam per millimeter at 158 μm. Figure 1 illustrates our detector design. Each Ge : Ga crystal, (a), is a 1 mm cube centrally placed in a pillbox-shaped integrating cavity whose walls are a 4.5 mm hole drilled through a 1 mm thick wafer of aluminum. The base of each cavity is formed by a 50 μm thick piece of stainless steel stock, (b). The aluminum wafers and stainless stock are both plated with a 32 μm thick layer of copper and then soldered together. The copper plating serves as a cushioning pad for the Ge : Ga detectors along the stress axis, minimizing the possibility of crystal breakage due to unavoidable imperfections in the Ge : Ga crystal and stainless steel surfaces. Each detector is placed to within about 50 μm of the center of its cavity and fixed with indium solder. The corners of the detectors are centered with respect to the entrance pinholes to ensure that the first pass of reflected radiation off the crystal is trapped by the integrating cavity and not directly reflected out through the entrance aperture. The aluminum wafers are then stacked such that the bottom of one detector cavity forms the top of the cavity below. The top cavity is capped by the stainless steel top of the detector housing. The entire assembly is gold plated to enhance reflectivity and prevent corrosion.

The detector housing itself is maintained at constant voltage bias, while the signal end of the detector is electrically isolated from the housing by a 75 μm thick sheet of mica, (c). The
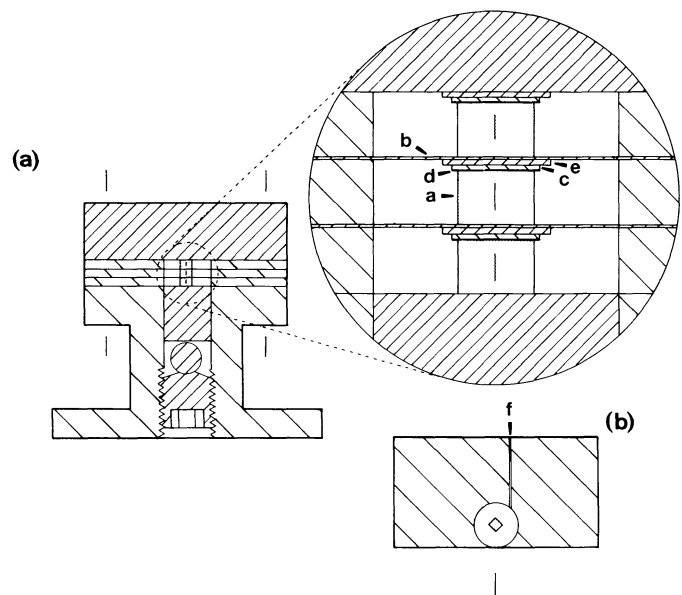

FIG. 1.—(a) Cutaway drawing for the three-element stressed detector described in the text. The inset is an enlarged view of the detector cavities themselves. (b) Top view of a single detector "wafer" show with the detector installed. The signal wire is retained by a 250 μm wide, 250 μm deep groove, (f), in the aluminum wafer.

electrical connection is obtained with a 25 μm thick sheet of brass, (d), which also serves as a stress pad for the detector. Brass pads have an advantage over copper pads in that they cushion adequately but do not extrude under stress nearly as much as copper pads (Beeman et al. 1989). The brass pad has a 75 μm diameter high thermal impedance (Constantan) wire indium-soldered at one corner to complete the electrical circuit. A 2 mm diameter, 100 μm thick disk of stainless steel, (e), is fixed to the bottom of each detector wafer, which prevents "drumhead" distortions of the stainless steel bottom plate of the cavities as the stress is applied. These distortions would result in nonuniform stress, manifesting itself as a slow responsivity onset at long wavelengths, and nonoptimal response over a broad band. Stress is applied through the entire stack of three detectors with a single one-quarter inch—28 thread set screw and delivered through a 4.5 mm diameter piston 5 mm long. Screw torque is decoupled with a one-eighth inch (3.2 mm) stainless steel ball bearing. The body of the detector is constructed of aluminum alloy which ensures good thermal conductivity and results in a large amount of differential thermal contraction between the housing and the stainless steel set screw, ball bearing, plunger, and germanium crystal stack. Thus, cooling the detector increases the stress along the detector array axis.

The initial stress on the detector is set at room temperature by measuring the DC impedance of the detector as the screw is tightened. We find that lowering the impedance to about 85% of its unstressed value results in a responsivity curve which peaks at about 158 μm for this type of detector housing. The differential contraction in the detector housing during cooling will then result in a pressure of about 5×10^9 dyn cm^{-2} at 2 K.

3.2. Performance

The operating characteristics of the three-channel system are similar to the single channel system previously used in the spectrometer (Table 2). At 158 μm, the detector response is ~ 4 A W^{-1} for each channel at the optimal bias voltage (10 mV across the 1 mm interelectrode distance). The detector sensitivity as a function of bias is nearly flat near the optimal bias point, and therefore all detectors may be operated at their optimal sensitivity with a common detector bias. The cutoff wavelengths for each of the three detectors is nearly identical to that of a single stressed detector (~ 210 μm), and the onset is consistent with good uniform stress across the three channels.

We measure a system NEP at 158 μm for the central channel of our array which is as good as our best single-channel NEP (~ 2 to 3×10^{-15} W Hz$^{-1/2}$ at 40 km s^{-1} resolution). The side channels have a somewhat higher NEP due to walkoff of the FIR radiation through the Fabry-Perot (cf. Poglitsch et al. 1991a). This problem is not severe at 100 km s^{-1} resolution (factor of 1.3) but rapidly worsens as the divergence limit of the side channel resolution (32 km s^{-1}) is approached. The transmission of the entire optical path in the Fabry-Perot spectrometer is of the order 16% (Lugten 1987). With this transmission, and given the background limited performance of the spectrometer, we calculate a quantum efficiency of 20% for each of the detectors.

The detectors are kept at ~ 2.2 K by pumping on the liquid helium bath. At these temperatures, the dark current is $\sim 3 \times 10^7$ electrons s^{-1}. Due to the high background environment on the KAO telescope (equivalent to a 240 K graybody of emissivity 25%), this dark current is an insignificant effect ($\sim 10\%$ of the KAO background). We use a standard matched dual J-FET (2N6484) transimpedance amplifier and 2×10^9 Ω ELTEC model 104 load resistors. The silicon J-FETs are mechanically coupled to the liquid helium temperature work surface with thin-wall fiberglass tube and heated to an 80 K operating temperature with a 1 kΩ carbon resistor. The detector is shielded from radiation emitted by the heated J-FET assembly with a liquid helium temperature copper house around the J-FET "tower." The transimpedance amplifier is essentially free of microphonic pickup.

For a 45" pinhole, the divergence of the beam limits the maximum attainable spectral resolution (zero transmission) of our spectrometer to 8 km s^{-1} for the central channel (see Lugten 1987). The light comes in at an angle for the off-axis detectors, and they are more severely affected by the angular divergence within the beam. We find the divergence limit for our side channels to be 40 km s^{-1} through measurements of narrow [C II] lines in astronomical sources (Orion and W3). This is close to what we calculate theoretically. Therefore, the side channels will always have a spectral resolution which is 32 km s^{-1} worse than the central channel and transmit at a frequency ~ 30 km s^{-1} to the blue of the central channel. This result is repeatedly checked in flight by observing calibration lines in all three channels.

The 45" pinhole size yields a beam size of 55" (FWHM) on the sky, including the effects of diffraction of the KAO tele-

<div align="center">TABLE 2</div>

<div align="center">COMPARISON OF THREE-ELEMENT ARRAY WITH SINGLE DETECTOR</div>

DETECTOR	CUTOFF λ (μm)	OPTIMAL BIAS (mV)	RESPONSE[a,b] (A W^{-1})	Unvignetted[b] (100 km s^{-1})	Inflight[d] (100 km s^{-1})	Inflight[d] (40 km s^{-1})
Single detector	210	15	4.6	3.9	3.9	2.5
Three-element array:						
1	215	10	4.1	4.0	5.6	...
2 (central	220	10	4.9	3.6	3.6	2.3
3	205	10	4.0	3.9	4.6	...

[a] At optimal bias.

[b] For a direct pass through the system; i.e., taking into account known vignetting in the system for the side channels of the three-channel detector, but not correcting for walk-off in the Fabry-Perot.

[c] In units of 10^{-15} W Hz$^{-1/2}$, at 158 μm, at the quoted spectral resolutions (FWHM).

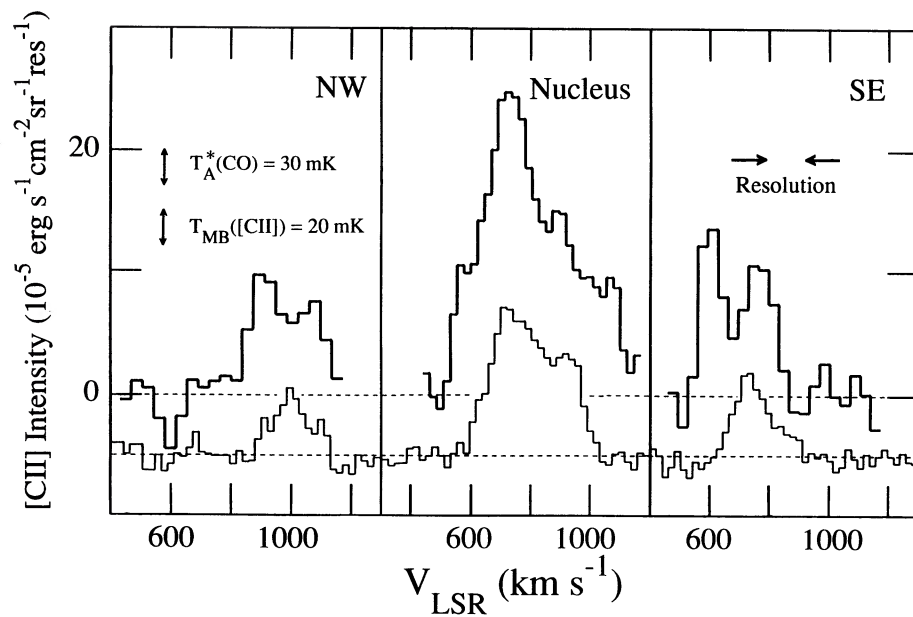[d] Referred to the sky, i.e., including all losses.

FIG. 2.—Spatially multiplexed [C II] spectrum of the starburst SB(s)ab pec galaxy NGC 2146 obtained on the first flight with our three-element stressed detector array. The side channels are located ±55″ from the center (nuclear) position at a position angle of 118°. Total integration time is 22 minutes. Superposed on the [C II] scans are the ^{12}CO (1 → 0) spectra obtained by Young et al. (1988) with a 45″ beam. The far-infrared continuum level has been subtracted off. T_{MB}([C II]) is the main beam Rayleigh-Jeans brightness temperature scale for the (spectrally resolved) [C II] lines. The [C II] data have been Hanning-smoothed once.

scope. The array spacing is 55″ along a rotation angle of 67° with respect to the vertical. This angle, together with the rotation angle of the source for the alt-azimuth mounting of the KAO, determines the absolute positions of the side channels relative to the bore-sighted central detector. The coordinates given in Table 1 are those of the galactic nucleus at which the central detector was pointed. The average position angle of the side channels for the galaxies mapped with the new array are

given in Figures 2–5. Note that for northern sources the side channels may rotate on the source by as much as 20° during a 45 minute integration.

Electrical crosstalk, determined through laboratory measurements, is ~1% between adjacent detectors. The optical crosstalk between detectors, i.e., that percentage of the signal from a point source in one channel which shows up due to diffraction as an edge of the beam signal in the next adjacent
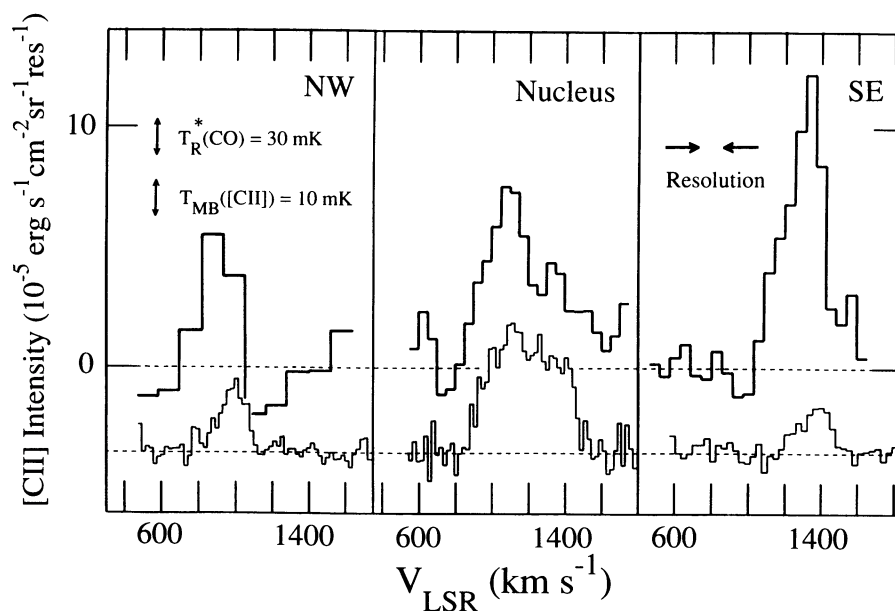
FIG. 3.—The same as Fig. 2 but for the SB(s)c galaxy NGC 3079. The position angle of the side channels is 4°. Total integration time is 31 minutes. The ^{12}CO (1 → 0) spectra (this work) were taken with the NRAO 12 m telescope (55′ beam).
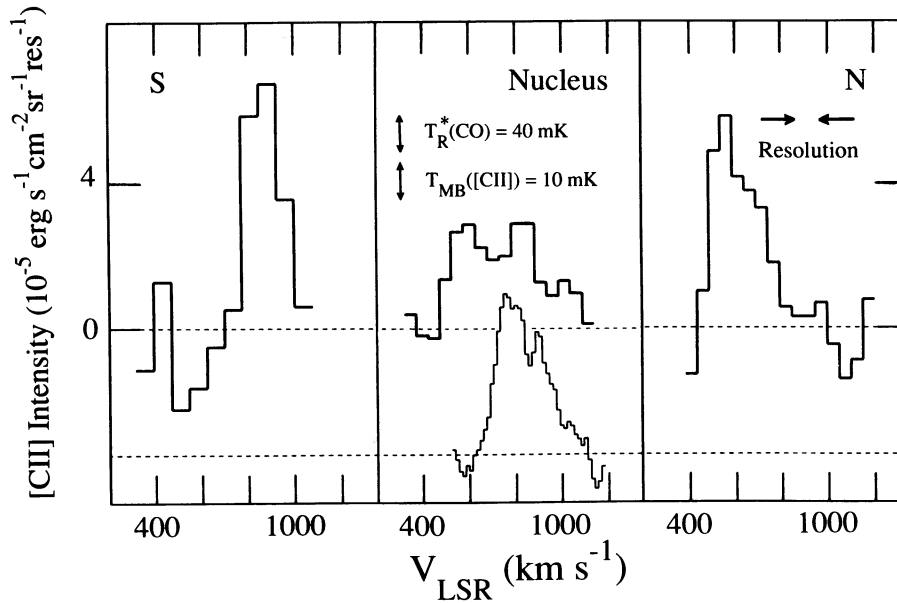
STACEY ET AL.

FIG. 4.—The same as Fig. 2 but for the Sb pec galaxy NGC 3628. The position angle of the side channels is 166°. Total integration time is 38 minutes. The ^{12}CO $(1 \rightarrow 0)$ spectrum is from Young, Tacconi, & Scoville (1983) (50″ beam).

channel, was determined through in flight measurements of Jupiter (42″5 diameter). We deconvolve the finite size of Jupiter using the calculations of Harris (1988), to determine the point source beam overlap. For immediately adjacent channels it is 10%, and for channels two beams away it is 2%. These numbers are in excellent agreement with laboratory measurements of the beam profiles for the individual channels.

4. RESULTS

We detected [C II] radiation from 11 of the 13 galaxies newly investigated. Six of these were detected with the new spatial array. Of these six, four (NGC 2146, NGC 3079, NGC 3628, and NGC 4736) are spatially extended objects whose rotation angles during observations permitted three point mapping with the array. Figures 2–5 show the [C II] spectra obtained of these sources. For comparison, we superpose the ^{12}CO $(J = 1 \rightarrow 0)$ spectra at about the same spatial resolution and observed at the same nominal position (within the combined pointing errors). Figures 6–12 display the [C II] spectra of the other detected galaxies together with the corresponding CO spectrum when available. The [C II] line is spectrally resolved in all of these sources except NGC 3690. Figure 13a displays
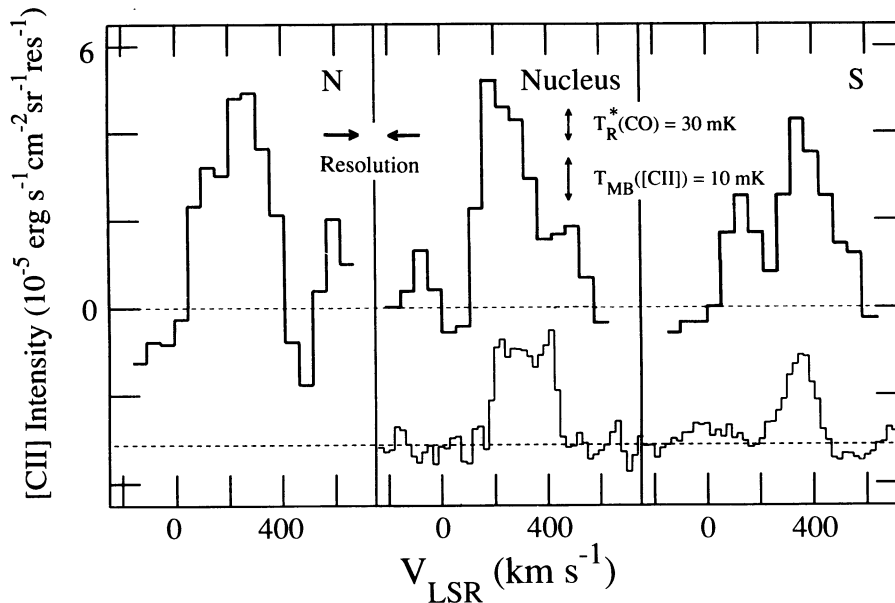
FIG. 5.—The same as Fig. 2 but for the RSA(r)ab galaxy NGC 4736. The position angle of the side channels is 8°. Total integration time is 25 minutes. The ^{12}CO $(1 \rightarrow 0)$ spectra (this work) were taken with the NRAO 12 m telescope (55″ beam).
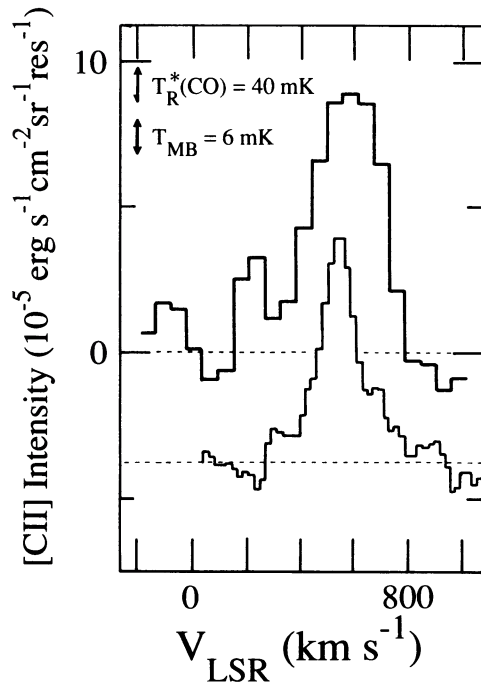
FIG. 6.—[C II] spectrum obtained on the nucleus of the SA(s)b galaxy NGC 891. Total integration time is 40 minutes. As for Fig. 2, the far-infrared continuum level has been subtracted off, and T_{MB}([C II]) is the main beam Rayleigh-Jeans brightness temperature scale for the (spectrally resolved) [C II] lines. The ^{12}CO $(1 \rightarrow 0)$ spectrum (C. E. Walker, personal communication) was taken with the NRAO 12 m telescope (55″ beam).
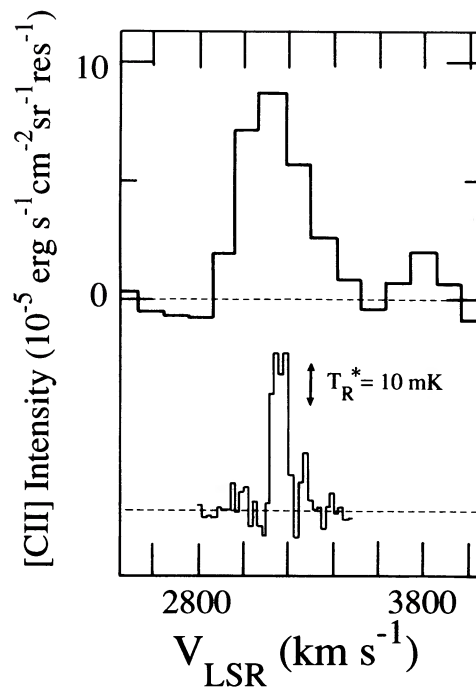
FIG. 8.—The same as Fig. 6 but for the IBm pec galaxy pair NGC 3690/IC 694. The [C II] beam was peaked on IC 694 but is sufficiently large to encompass both components. Total integration time is 40 minutes. The superposed ^{12}CO $(1 \rightarrow 0)$ spectrum is from Sanders & Mirabel (1985) (60″ beam).
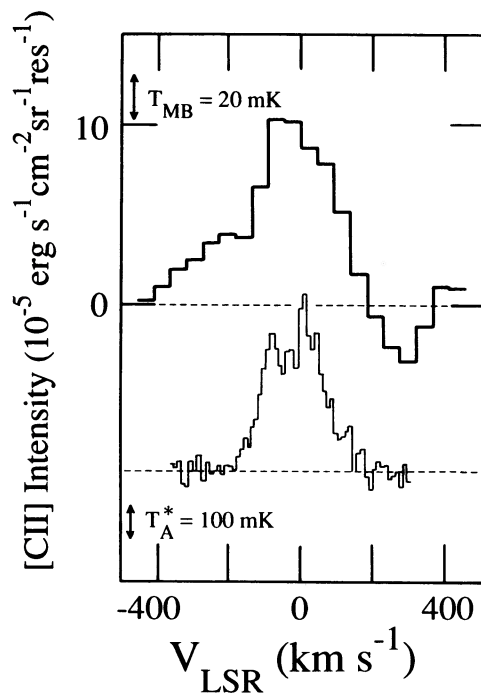
FIG. 7.—The same as Fig. 6 but for the SAB(rs)bc galaxy Maffei II. Total integration time is 40 minutes. The superposed ^{12}CO $(1 \rightarrow 0)$ spectrum is from Sargent et al. (1985).
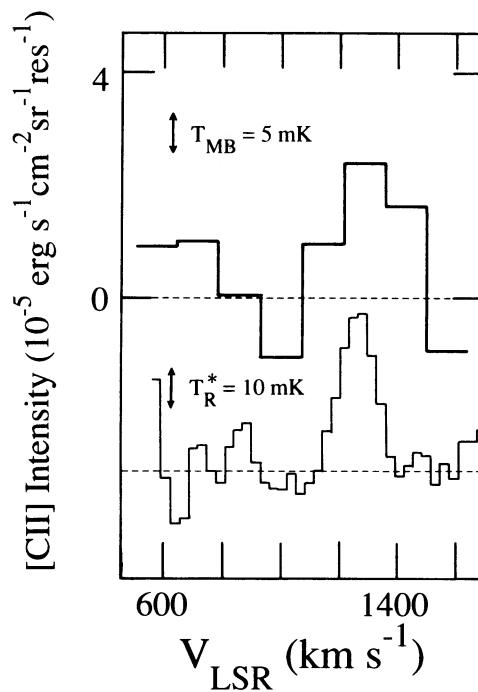
FIG. 9.—The same as Fig. 6 but for the SA(s)b galaxy NGC 4565. The data are not smoothed. Total integration time is 40 minutes. The superposed ^{12}CO $(1 \rightarrow 0)$ spectra (this work) were taken with the NRAO 12 m telescope (55″ beam).
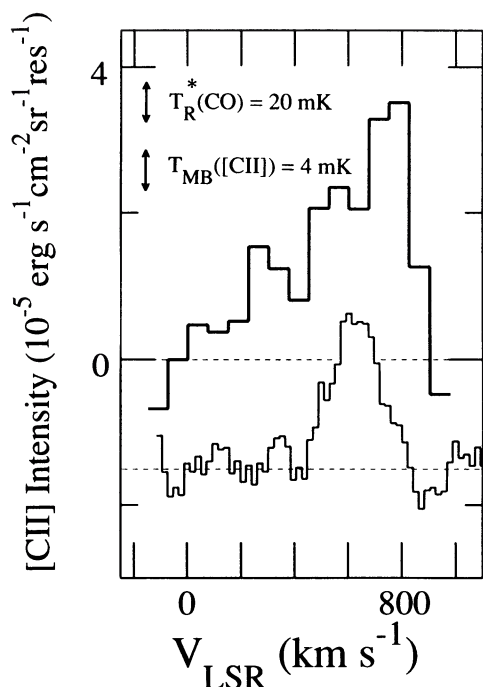
FIG. 10.—The same as Fig. 6 but for the SA(s)c galaxy NGC 5907. Total integration time is 40 minutes. The superposed ^{12}CO ($1 \rightarrow 0$) spectra (this work) were taken with the NRAO 12 m telescope (55" beam).

FIG. 11.—The same as Fig. 6 but for the IO pec galaxy NGC 6240. This spectrum is a composite of two data sets whose total integration time is 80 minutes. The superposed ^{12}CO ($1 \rightarrow 0$) spectrum is from Sanders & Mirabel (1985) (45" beam).
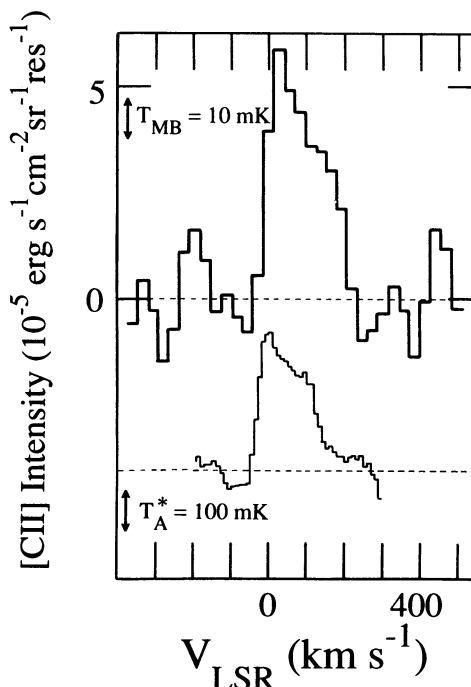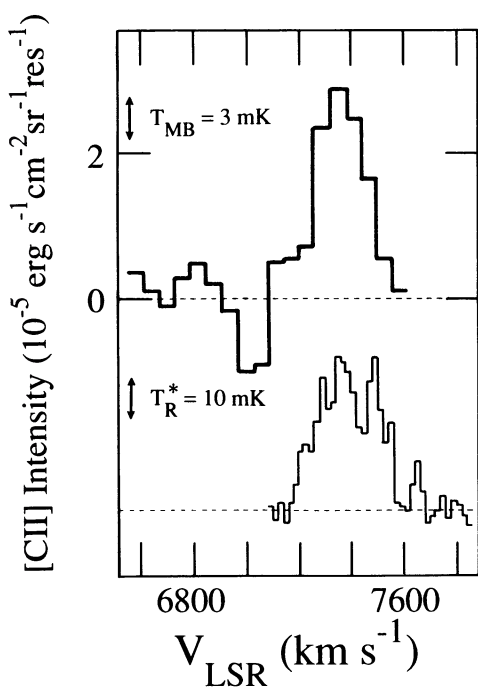

FIG. 12.—The same as Fig. 6 but for the SAb(rs)cd galaxy NGC 6946. Total integration time is 60 minutes. The superposed ^{12}CO ($1 \rightarrow 0$) spectra is from Young & Scoville (1984) (50" beam).

the integrated [C II] line intensity map of M82, and Figures 13b–13d are the individual velocity channel maps. The [C II] strip scans (heavy lines) of M82 across the major and minor axis are displayed as Figures 14a and 14b, respectively. We have superposed our FIR point source beam profiles (dashed lines) and the integrated ^{12}CO ($1 \rightarrow 0$) strip scans (light lines) of Young & Scoville (1984).

Table 3 lists the [C II] integrated line intensities from the nuclear regions of the galaxies we observed, together with the [C II] intensities observed in the mapped galaxies using the off-axis beams, and the [C II] intensity integrated over the inner 60" radius of M82. Table 3 also lists the properties derived from the [C II] line including minimum C$^+$ column densities [obtained in the high-density ($n_H \gg 2 \times 10^3$ cm^{-3}), high-temperature ($T \gg 91$ K) limit (see CGTW, Appendix B)], the inferred minimum column densities of hydrogen nuclei (assuming C$^+$/H $= 3 \times 10^{-4}$), and the [C II] luminosity of the source. Also included in Table 3 are the far-infrared properties of the sources, corrected when possible to our 55" beam. For completeness, the data from the gas-rich galaxies from CGTW, [C II] data from the 30 Doradus region of the Large Magellenic Cloud (Storey et al. 1991a) and selected Galactic regions (Table 5) are also included. The main results are as follows.

4.1. Brightness of the [C II] Line

The [C II] luminosity of the nuclear regions ranges from $5.0 \times 10^6 L_\odot$ in the nearby Sab galaxy NGC 4736 to $9.0 \times 10^8 L_\odot$ in the distant IR luminous galaxy NGC 6240. The (spectrally resolved) [C II] line-to-158 μm continuum ratio is typically in excess of $5:1$. Between 0.1% and 1% of the FIR luminosity of the program galaxies emerges in the 158 μm line (Table 3, col. [9]). This ratio does not show any clear dependance on galactic spectral type or FIR luminosity. For com-
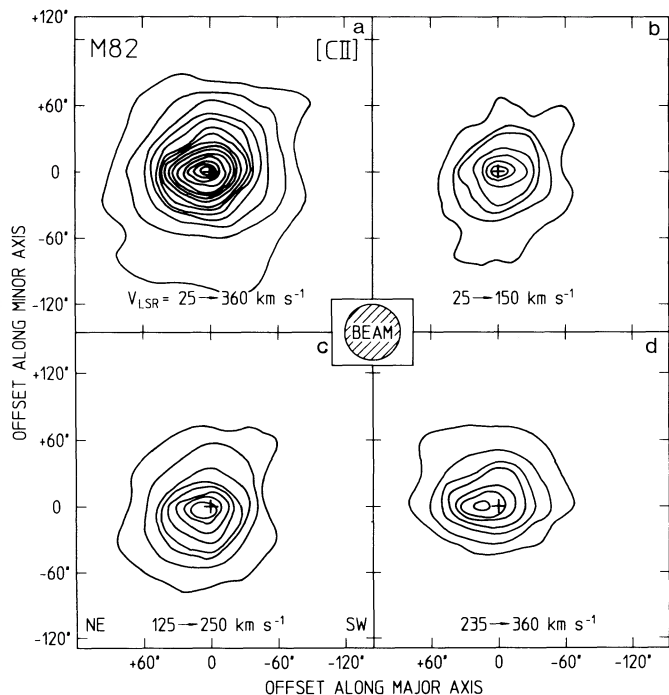
FIG. 13.—Integrated [C II] line intensity (a) and velocity channel maps (b)–(d) of the Ir II galaxy M82 taken with our three-element array in 1988 January. (a) The integrated line intensity map is composed of the composite flux from (b)–(d). The contour interval (4 σ) is 1.09×10^4 ergs s^{-1} cm^{-2} sr^{-1} and the peak intensity is 1.64×10^{-3} ergs s^{-1} cm^{-2} sr^{-1}. (b)–(d) Channel maps taken with 80 km s^{-1} resolution at center velocities of (b) 90, (c) 190, and (d) 295 km s^{-1}. The maps are sampled every 30″ in the inner 90″ (major axis) by 80″ (minor axis) regions by the central channel. The side channels (position angle 117°) thus served to further increase the sampling of the inner regions plus to extend the map borders by 49″ along the major axis and 25″ along the minor axis. The contour interval (3.5 σ) is 1.54×10^{-3} ergs s^{-1} cm^{-2} sr^{-1} res^{-1}.

parison, the [C II] luminosity of the Galaxy is estimated to be ~ 4–$6 \times 10^7 L_{\odot}$ (Stacey et al. 1985; Stacey 1985; Shibai et al. 1991) or $\sim 0.4\%$ of the Galactic FIR luminosity (Cox & Mezger 1987).

4.2. Spatial Distribution

4.2.1. Spectrally Scanned Galaxies

For the galaxies for which we have obtained three-point maps, the [C II] emission usually peaks toward the nucleus but remains detectable in the extranuclear regions. At a galactocentric radius of 3.8 kpc, the intensity of the [C II] line from the starburst galaxy NGC 2146 falls to only $\sim 25\%$ its nuclear value. The mapping of the IR-luminous galaxies M82 (see also below), M83, and NGC 1068 in CGTW give consistent results: *the [C II] line intensities are strongly peaked toward the nuclear (presumably starburst) regions of infrared-bright galaxies.* In contrast, the [C II] distribution is noticeably flatter for the less infrared active galaxies NGC 3079, NGC 3628, and NGC 4736 over similar galactocentric scales (see also the data for M51 in CGTW). This apparent difference between the infrared-active and less active galaxies is the result of enhanced [C II] emission in the nuclear regions of the FIR-active galaxies. The [C II] intensities from the galactic disks of both types of galaxies are more comparable.

The [C II] surface brightness of normal (i.e., "nonstarburst") galaxies is comparable to that of the Galaxy. The [C II] bright-

ness near the center of the Galaxy is $\sim 1.7 \times 10^{-3}$ ergs s^{-1} cm^{-2} sr^{-1} (Genzel et al. 1985; Okuda et al. 1989) and maintains a level near 10^{-3} ergs s^{-1} cm^{-2} sr^{-1} out to at least a galactocentric radius of 1.4 kpc (Stacey et al. 1985; see also Shibai et al. 1991). We compare the Galactic surface brightness to that of the two edge-on Sb galaxies in our sample, NGC 891 ($i \geq 87°5$; Sancisi & Allen 1979) and NGC 3628 ($i \sim 89°$; de Vaucouleurs, de Vaucouleurs, & Corwin 1976). Assuming the scale height for the [C II] emission in the Galaxy is 60 pc (Stacey et al. 1985) the Galactic [C II] surface brightness scales to intensities of 5–8×10^{-5} ergs s^{-1} cm^{-2} sr^{-1} in our 55″ beam at the distance of NGC 891 (~ 9.6 Mpc), and 7–11×10^{-5} ergs s^{-1} cm^{-2} sr^{-1} at the distance of NGC 3628 (~ 6.7 Mpc). The observed intensities of the [C II] line are 10.0 and 5.5×10^{-5} ergs s^{-1} cm^{-2} sr^{-1} in the inner (55″) 1.9 kpc and 0.9 kpc regions of NGC 891 and NGC 3628, respectively. Thus, the [C II] line brightness of the nuclear regions of the two Sb galaxies are comparable to that of our Galaxy.

4.2.2. M82

Figures 13 and 14 demonstrate that the [C II] emission from M82 is significantly more extended than our 55″ beam. [C II] emission may be traced to a galactocentric radius of at least 120″ (1.9 kpc) along both the major and the minor axis. Inspection of the single velocity channel maps (Figs. 13b–13d) reveals that the [C II] emission traces the rotation curve along the major axis in the inner galaxy changing from blueshifted emission in the west to redshifted emission in the east. This rotation pattern is consistent with the previous [C II] work of Lugten et al. (1986b) and the ^{12}CO (1 → 0) rotation pattern obtained with beams of similar sizes (e.g., Olofsson & Rydbeck 1984; Young & Scoville 1984). Thus, much of the [C II] emission in the inner regions of M82 is probably associated with the rotating molecular disk or ring.

The integrated [C II] emission (Fig. 13a) is peaked on the nucleus. Along the major axis, the [C II] distribution is resolved with our beam indicating an intrinsic diameter of 45″ FWHM. The central emission region is unresolved along the minor axis (diameter < 20″; Fig. 14). The [C II] emission detected along the major axis scan is consistent with emission from this broad central source only. However, there is extended emission along the minor axis which is clearly not associated with the central unresolved source. This emission is present both above and below the plane of the galaxy, at distances of about 1 to 1.5 kpc from the midplane and is especially pronounced in the 190 km s^{-1} velocity channel map (Fig. 13c). This extended [C II] emission may be associated with the filamentary features observed in the optical recombination lines and may represent gas which is being expelled from the nuclear regions of the galaxy (cf. Lugten et al. 1986b).

4.3. Comparison with ^{12}CO (J = 1 → 0) Emission

4.3.1. Distribution

Figures 2–12 demonstrate the good agreement between our measured [C II] line profiles and those of ^{12}CO (1 → 0). The small velocity shifts and profile differences between these lines are probably due to the combined pointing errors between the [C II] and CO observations.

The three channel maps displayed in Figures 2–5 shown that the [C II] and ^{12}CO (1 → 0) have similar large scale spatial distributions for a wide variety of galactic spectral types ranging from the early gas-poor system NGC 4736 through the intermediate to late spiral galaxies NGC 3079 and NGC 3628

TABLE 3

[C II] Line Intensities and Far-Infrared Properties of the Galaxy Sample

Galaxy	Distance[a] (Mpc)	Linear Size of Beam (FWHM)	I[CII] (10^-5 ergs s^-1 cm^-2 sr^-1)	L[CII] (10^7 L_⊙)	$N_{C^+}^{min(b)}$ (10^16 cm^-2)	$N_H^{min(b)}$ (10^20 cm^-2)	L_FIR (10^9 L_⊙)	L[CII]/L_FIR	$\chi_{FIR}^{(c)}$	$\Phi^{(d)}$	$T_D^{(e)}$ (K)	Reference (Distance; FIR; [CII])
NGC 660	12.	3.2kpc	≤3.9 (3σ)	≤1.5	≤2.5	<0.8	22.	≤7 × 10^-4	280	0.3	38	1;2
NGC 891	9.6	2.6	10.0±1.1	2.5	6.3	2.1	9.	3.1 × 10^-3	180	0.4	34	3;4
Maffei II	5.	1.3	19.0±1.2	1.3	12.	4.0	4.2	2.9 × 10^-3	310	0.3	43	5;2
NGC 2146 NW SE	14.4	3.8	39.0±0.8 9.9±1.8 10.2±1.3	22. 5.6 5.7	25. 6.3 6.5	8.2 2.1 2.2	49.	4.6 × 10^-3	430	0.3	40	6;2
M82(55")[f] (120") (r=90")	3.3	0.88 1.9 0.88	165 69 6.7	4.9 6.4 0.20	100 44. 4.1	37. 15. 1.5	28. 28. 2.6	1.8 × 10^-3 2.3 × 10^-3 7.6 × 10^-3	4700 1000 440	1.6	49	12;2
NGC 3079 NW SE	16.	4.3	11.3±0.9 7.1±2.5 13.9±1.4	7.9 4.9 9.7	7.2 4.5 8.8	2.4 1.5 2.9	28.	2.8 × 10^-3	200	0.4	35	7;8
NGC 3109	1.7	0.5	≤3.4 (3σ)	≤0.03	≤2.2	<0.7	0.02	≤2 × 10^-2	13	0.1	36	9;10
NGC 3628 S N	9.6	2.6	7.9±0.9 4.4±1.4 5.2±0.7	2.0 1.1 1.3	5.0 2.8 3.3	1.7 0.9 1.1	7.2	2.9 × 10^-3	140	0.3	34	11;2
NGC 3690 /IC 694	44.	11.8	9.4±1.5	49.	5.9	2.0	330.	1.5 × 10^-3	310	0.05	46	11;4
NGC 4565	10.2	2.7	3.0±1.0	0.85	1.9	0.6	3.0	2.8 × 10^-3	53	0.05	37	12;10
NGC 4736 N S	5.	1.3	7.3±0.8 6.1±1.5 5.3±0.9	0.50 0.41 0.36	4.6 3.9 3.4	1.5 1.3 1.1	1.8 0.9 0.9	2.8 × 10^-3 4.7 × 10^-3 4.0 × 10^-3	130 67 67	0.15	36	12;4
NGC 5907	10.4	2.8	6.0±0.9	1.8	3.8	1.3	2.9	6.1 × 10^-3	49	0.2	29	11;10
NGC 6240	100	27.	3.3±0.66	90.	2.1	0.70	620.	1.5 × 10^-3	110	0.05	45	13;8
NGC 6946	11.	2.9	7.6±1.1	2.5	4.8	1.6	8.9	2.9 × 10^-3	140	0.5	32	12;4
NGC 1068	18.1	4.8	43[g]	38.	27.	9.	115.	3.3 × 10^-3	650	0.7	52	12;2;14
IC 342	1.8	0.48	30	0.26	19.	6.3	0.6	4.4 × 10^-3	340	0.3	46	15;2;14
LMC 30DOR	49kpc	13.0pc	95	6.2 × 10^-4	60.	20.	5.5 × 10^-3	1.2 × 10^-3	4200	...	65	16;17;18
NGC 5128 (Cen A)	5.0	1.33	29	2.0	18.	6.3	7.2	1.0 × 10^-3	1500	0.2	43	19;20;14
M51 (NGC 5194)	9.7	2.6	14	3.6	8.9	3.0	3.	1.2 × 10^-2	59	0.5	30	12;21;14
M51 HII		2.6	5	1.3	3.2	1.0	1.	1.3 × 10^-2	20	0.1	30	
M83 (NGC 5236)	5.4	1.4	47	3.7	30.	9.9	9.	4.1 × 10^-3	570	0.6	43	12;10,22 14

[a] Distances scaled to $H_0 = 75$ km s^-1 Mpc^-1.

[b] Minimum column densities calculated assuming the [C II] line is optically thin, the levels are populated in the high-temperature, high-density limit, and [C⁺]/[H] = 3 × 10^-4 (CGTW; Appendix B).

[c] $\chi_{FIR} = L_{FIR}/4\pi D^2 \Omega (2.0 \times 10^{-4}$ ergs s^-1 cm^-2 sr^-1), where D is the source-Earth distance, and Ω is the beam solid angle.

[d] $\Phi \equiv \chi_{FIR}/\chi_{UV} = \chi_{OBSERVED}/\chi_{THEORETICAL}$. The values for χ_{UV} are estimated from Fig. 18 and are accurate to about a factor of 2.

[e] Dust temperatures calculated from the FIR fluxes assuming a λ^{-1} grain emissivity law.

[f] Regions for M82. (55"): 55" beam centered on the nucleus. (120"): Average, integrated over the inner 120" diameter region (from Fig. 14). (r = 90"): Average of the four 55" beams at ±90" along the major and minor axis of the galaxy (from Fig. 13). For this region χ_{FIR} is derived by geometric dilution of the nuclear far-infrared flux.

[g] The line intensities from CGTW have been adjusted to agree with the intensity scale of this work.

References.—(1) Benvenuti, Capaccioli, & D'Ordorico 1975; (2) Rickard & Harvey 1984; (3) Sancisi & Allen 1979; (4) G. Engargiola, personal communication; (5) Spinrad et al. 1973; (6) Burbidge, Burbidge, & Pendergast 1959; (7) Nilson 1973; (8) IRAS PSC; (9) Carigan 1985; (10) Rice et al. 1988; (11) Sandage & Tammann 1981; (12) Sandage & Tammann 1975; (13) Distance from [C II] velocity; (14) Crawford et al. 1985; (15) McCall 1989; (16) Eastman & Kirshner 1989; (17) Werner et al. 1978; (18) Storey et al. 1991a; (19) Burbidge & Burbidge 1959; (20) Joy et al. 1988; (21) Smith 1982; (22) Telesco & Harper 1980.

to the starburst galaxy NGC 2146. Figure 14 demonstrates the good spatial correlation between [C II] and the CO distributions over the inner 40" radius (0.64 kpc) regions for the starburst galaxy M82. A good spatial correlation has previously been demonstrated in the cases of M83 and NGC 1068 (CGTW), for several Galactic OB star formation regions (e.g.,

M42 [Stacey et al. 1991; Genzel & Stacey 1985], M17 [Stutzki et al. 1988; Matsuhara et al. 1989]) and over Galactic giant molecular clouds (OMC-1 [Stacey et al. 1991], M17 SW [Stutzki et al. 1988; Matsuhara et al. 1989]) and through the plane of our Galaxy (Stacey et al. 1985; Stacey 1985; Shibai et al. 1991).
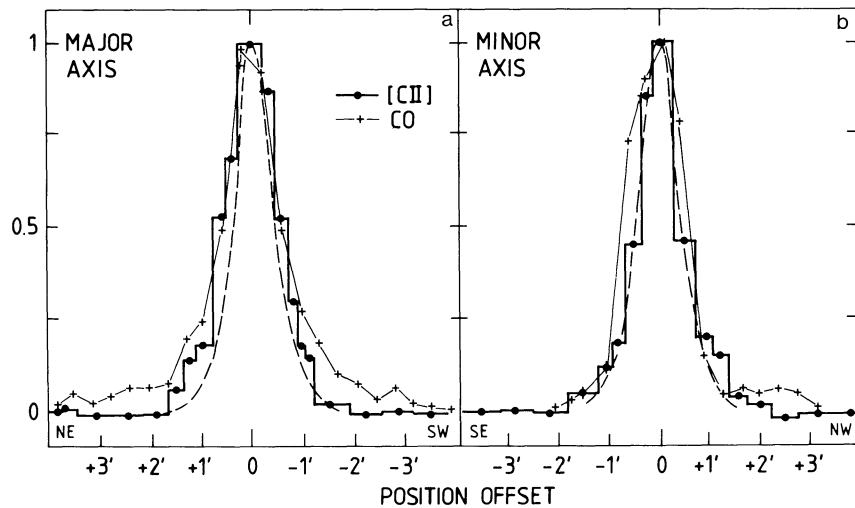
FIG. 14.—Integrated [C II] intensity cuts (*solid lines*) across the major (*a*) and minor (*b*) axis of M82. We have superposed our FIR point source beam profiles (*dotted lines*) and the ^{12}CO (1 → 0) integrated intensity cuts of Young & Scoville (1984) (50″ beam).

4.3.2. Integrated Line Intensity

Figure 15*b* plots the integrated [C II] line intensity from the nuclear regions of the galaxy sample against the ^{12}CO (1 → 0) line intensities for beams of similar sizes (Table 4, col. [2]). There is a good correlation between CO and [C II] for most of the galaxies sampled. A notable exception is the 30 Doradus region of the LMC, a very low metallicity galaxy. We defer discussion of this object until § 5.5. The correlation becomes much tighter if the galaxies are divided into two groups which are distinguished by their inferred dust temperatures (Table 3, col. [12]). Galaxies with dust temperatures in excess of 40 K are plotted as asterisks and those less than 40 K as open triangles in Figure 15. Selection by elevated dust temperature generally picks out those galaxies believed to display starburst activity. This is not surprising, as the higher UV fields found in starburst galaxies will elevate the equilibrium dust temperature. The warm dust galaxies (with the exception of NGC 6240 [*filled triangle*]) display a strikingly tight correlation between the integrated [C II] and ^{12}CO (1 → 0) line intensities. These galaxies have a constant [C II]-to-CO intensity ratio of 6300.[5] For the cool dust galaxies this ratio is not only significantly lower (∼ 2000) but shows considerably more scatter.

We also plot the integrated [C II] line intensities as a function of the ^{12}CO line intensities for a wide variety of Galactic regions (Table 5) in Figure 15. Galactic OB star formation or H II regions are plotted with filled circles and the non–OB star-forming molecular clouds with open circles. The star-forming regions in the galaxy fall closely along the same correlation line (Fig. 15*a*) as do the high dust temperature (starburst) galaxies. Again, as for the nonstarburst galaxies, the non–OB star-forming molecular clouds have significantly less [C II] line radiation relative to that of ^{12}CO and also display much more scatter in that ratio (Fig. 15*b*).

The correlation between the integrated [C II] and ^{12}CO (1 → 0) line intensities is reasonably tight for Galactic OB star formation or H II regions and external starburst galaxies. The correlation is particularly striking in that it extends nearly three orders of magnitude in terms of line intensity and nine

[5] Correcting the CO observations for main beam efficiency (∼0.65%) $I_{[C II]}/I_{CO}$ ∼ 4100.
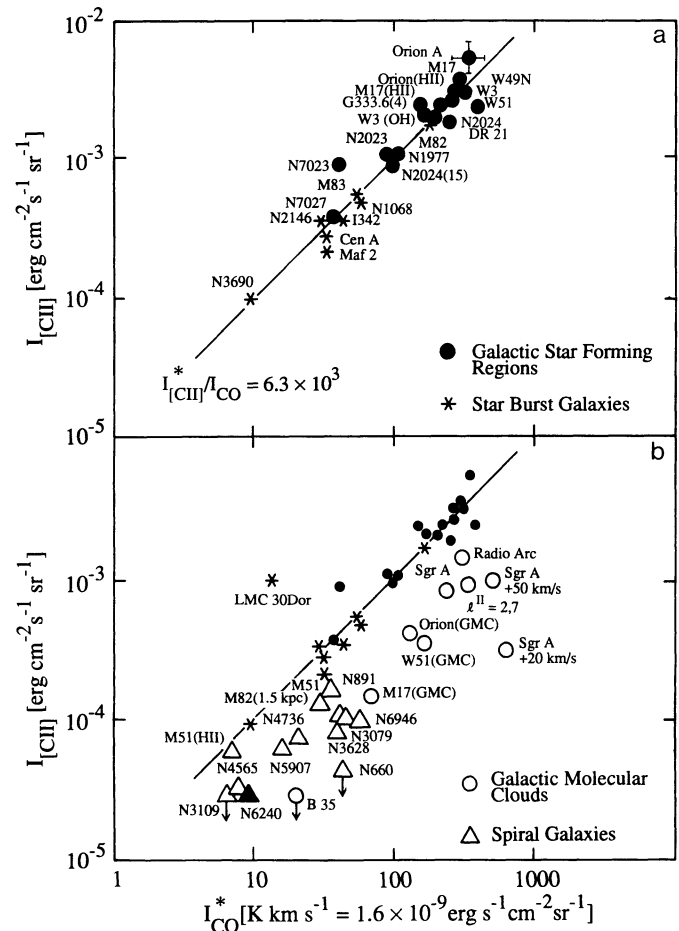
FIG. 15.—(*a*) Correlation between the integrated line intensities of [C II] and ^{12}CO (1 → 0) for Galactic and extragalactic sources. The CO line intensities are normalized to the "Kitt Peak scale" ($T_R^* = 72$ K for Orion). To convert to main-beam brightness temperature, multiply by 1.5. A typical error bar is shown for M42. High dust temperature ($T_d \geq 40$ K) (starburst) galaxies are marked as asterisks, nonstarburst galaxies as open triangles, Galactic OB star formation regions by filled circles, and non–star-forming Galactic clouds by open circles. The solid line represents a best fit to the starburst galaxies and Galactic OB star formation regions ($I_{[C II]}/I_{CO}^* = 6300$).

TABLE 4

Comparison of the [C II] Line Emission with the ^{12}CO $(1 \rightarrow 0)$ and H I 21 Centimeter Line Emission for Galaxies

Galaxy	I^*_{CO} (a)	N^{min}_{CO} (b)	$N^{min}_{H_2}$ (CO)	$N^*_{H_2}$ (c) (CO)	$I_{[CII]}/I^*_{CO}$ (d)	$\frac{N^{min}_H (C^+)}{N^{(CO)}_{H_2}}$ (e)	N^{21cm}_{HI} (e)	21 cm Beam	$\frac{N^{min}_H (C^+)}{N^{21cm}_{HI}}$	M_{C^+}	M_{C^+}/M_{gas}	Reference
	(K km s^{-1})	(10^{16}cm^{-2})	(10^{20}cm^{-2})	(10^{20}cm^{-2})			(10^{20}cm^{-3})			($10^7 M_\odot$)		(CO;HI)
NGC 660	42.7	11.8	14.7	128	≤600	≤0.01 - 0.05	15 e	3.1'	<0.05	≤0.081	≤0.024	1;2
NGC 891	41.4	11.4	14.3	124	1500	0.013 - 0.15	60 e	24.7" × 36.8"	0.04	1.33	0.01 - 0.03	3;4
Maffei II	33.1	9.1	11.4	99	3800	0.029 - 0.35	31 e	2'	0.13	0.69	0.02 - 0.09	5;6
NGC 2146	34.	9.4	11.7	102	7200	0.080 - 0.70	1.3e	72" × 52"	6.31	11.6	0.07 - 0.39	7;8
NW	6.9	1.9	2.4	21	9000	0.100 - 0.87	6.0e		0.35	3.0	0.07 - 0.20	
SE	9.0	2.5	3.1	27	7100	0.082 - 0.71	7.0e		0.31	3.1	0.06 - 0.18	
M82 (55")	170.	46.9	58.6	510	6100	0.073 - 0.63	41 e	1'	0.90	2.8	0.06 - 0.27	9;10
(120")	80.	22.1	27.6	240	5400	0.063 - 0.54	36 e		0.42	3.4	0.05 - 0.19	
(r=90")	17.	4.9	5.9	51	2500	0.029 - 0.25	31 e		0.05	0.1	0.02 - 0.04	
NGC 3079	46.2	12.8	15.9	139	1500	0.017 - 0.15	10 e	48.0" × 39.5"	0.24	4.2	0.02 - 0.09	11;12
NW	9.7	2.7	3.3	29	4600	0.052 - 0.45	25 e		0.06	2.6	0.02 - 0.05	
SE	10.4	2.9	3.6	31	8300	0.094 - 0.81	25 e		0.12	5.1	0.05 - 0.10	
NGC 3109	≈7	1.9	2.4	21	≤3000	≤0.03 - 0.29	13 e	9'	<0.05	≤0.01	≤0.04	13;14
NGC 3628	40.4	11.1	13.9	121	1200	0.014 - 0.12	19 e	3'	0.09	1.08	0.01 - 0.05	15;16
NGC 3690	9.0	2.5	3.1	27	6500	0.061 - 0.54	56 a	2.5"	0.04	27.	0.02 - 0.04	1,17;18
NGC 4565	6.9	1.9	2.4	21	2700	0.029 - 0.25	16 e	35"	0.04	0.43	0.02 - 0.03	11;19
NGC 4746 N	20.2	5.6	7.0	61	2200	0.025 - 0.21	1.4e / 8.6e	25" × 38"	1.07 / 0.15	0.26 / 0.22	0.02 - 0.15 / ≤0.15	11;20
S	11.8	3.3	4.1	35	2800	0.031 - 0.27	8.6e		0.13	0.19	0.02 - 0.08	
NGC 5907	16.0	4.4	5.5	48	2300	0.027 - 0.24				0.97	0.03 - 0.24	11
NGC 6240	9.0	2.5	3.1	27	2300	0.026 - 0.23	38 a	2.5"	0.02	48.	0.01 - 0.02	1;18
NGC 6946	52.4	14.5	18.1	157	900	0.010 - 0.09	7.2e	40"	0.22	1.33	0.01 - 0.06	21;22
NGC 1068	56.5	16.6	20.7	180	4500	0.050 - 0.44				20.	0.05 - 0.44	21
IC 342	37.7	10.4	13.0	113	5000	0.056 - 0.49	1.5e	1.9' × 2.0'	4.20	0.14	0.05 - 0.31	5;23
LMC 30Dor	14.7	4.1	5.1	44	40000	0.46 - 3.9	33 e	15'	0.61	3.3×10^{-4}	0.21 - 0.35	24;25
NGC 5128 (Cen A)	30.	8.3	10.3	90	6100	0.070 - 0.61	8.5a	2.6" × 11.0"	0.74	1.08	0.06 - 0.25	26;27
M51 (NGC 5194)	31.8	8.8	11.0	95	2700	0.032 - 0.27	10 e	25" × 35"	0.30	1.94	0.03 - 0.12	28;29
M51 HII	7.1	2.0	2.4	21	4400	0.048 - 0.42	18 e	25" × 35"	0.06	0.65	0.03 - 0.05	
M83 (NGC 5236)	48.1	13.3	16.6	144	6100	0.062 - 0.54	11 e	2'	0.90	2.0	0.06 - 0.26	1,21;30

a $I^*_{CO} \equiv \int T^*_R dV$ (K km s^{-1}); CO data from the literature are typically scaled to $T^*_R = 72$ K on the BN-KL region of the Orion Nebula. Where large discrepancies occur in the published values, we take an average value.

b Assuming optically thin emission and $T_{kin} = 40$ K (CGTW; Appendix B); $[CO]/[H_2] = 8 \times 10^{-5}$ (Frerking, Langer, & Wilson 1982).

c Using N_{H_2}(cm^{-2}) = $3 \times 10^{20} I^*_{CO}$ (K km s^{-1}) (Bloemen 1989).

d 1 K km s^{-1} = 1.6×10^{-9} ergs s^{-1} cm^{-2} sr^{-1}.

e e = emission; a = absorption (assumes $T_s = 50$ K).

REFERENCES.—(1) Sanders & Mirabell 1985; (2) Bottinelli, Gouguenheim, & Paturel 1980; (3) C. E. Walker, personal communication; L. Sage, personal communication; (4) Sancisi & Allen 1979; (5) Rickard & Blitz 1985; (6) Wright & Seielstad 1973; (7) Young et al. 1988; (8) Briggs 1985. Note that there is significant absorption of the 21 cm line against the galactic nucleus; (9) Young & Scoville 1984; (10) Crutcher, Rogstad, & Chu 1978; (11) This work; (12) Irwin et al. 1987; (13) Rowan-Robinson, Phillips, & White 1980; (14) Huchtmeier, Seiradakis, & Materne 1980; (15) Young, Tacconi, & Scoville 1983; (16) Haynes, Giovanelli, & Roberts 1979; (17) Solomon & Sage 1988; (18) Dickey 1982; (19) R. Sancisi, personal communication in Richmond & Knapp 1986; (20) Bosma, van der Hulst, & Sulivan 1977; (21) Young & Sanders 1986; (22) Tacconi & Young 1986; (23) Newton 1980; (24) F. I. Israel, personal communication; (25) Rohlfs et al. 1984; (26) Eckart et al. 1991; (27) van der Hulst, Golisch, & Haschick 1983; (28) Scoville & Young 1983; (29) Shane 1975; (30) Rogstat, Lockhart, & Wright 1974.

orders of magnitude in terms of [C II] line luminosity ranging from $L_{[C II]} \sim 1 L_\odot$ in the planetary nebula NGC 7027 to nearly $10^9 L_\odot$ for the starburst galaxy NGC 3690.

4.4. Comparison with H I 21 Centimeter Emission

Column (8) in Table 4 lists the column density of atomic hydrogen observed toward the galaxy sample as determined from 21 cm line emission (labeled " e ") or absorption (labeled " a "). Values obtained with beam sizes (col. [9]) similar to the FIR beam are quoted whenever possible. Whenever both emission and absorption measurements are available in the literature, the value quoted is that obtained from emission. The column densities obtained from absorption measurements should be regarded as less reliable since they require the assumption of a level excitation (spin) temperature. Figure 16 plots the integrated [C II] line intensities of the galaxy sample as a function of the atomic hydrogen column density. We have included three representative bright Galactic H II regions. Also

TABLE 5

COMPARISON OF THE [C II], ^{12}CO (1 → 0) AND FIR CONTINUUM EMISSION FOR GALACTIC SOURCES

Region	Distance (kpc)	Linear Size of Region (FWHM)	$I_{[CII]}$ (10^{-4}ergs s^{-1} cm^{-2}sr^{-1})	$L_{[CII]}$ ($L_\odot$)	$L_{FIR}^{(a)}$ ($L_\odot$)	$L_{[CII]}/L_{FIR}$	$\chi_{FIR}^{(b)}$	$I_{CO}^{*(c)}$ (K km s^{-1})	$I_{[CII]}/I_{CO}^*$	Reference ([CII];FIR;CO)
W3	2.4	0.64pc	25.	40.	2.0×10^5	2.0×10^{-4}	6.4×10^4	290	5400	1;2;3
		3.8	7.2	260.	1.0×10^6	2.6×10^{-4}	1.4×10^4	100	4500	4;5;6
W3(OH)	2.4	0.64	10.	16.	8.7×10^4	1.8×10^{-4}	2.8×10^4	110	5700	1;7;8
NGC 1977	0.45	0.12	12.	0.66	2.4×10^2	2.8×10^{-3}	2.2×10^3	94	8400	1;9;10
		0.12×0.79	7.6	2.2	6.3×10^2	3.5×10^{-3}	900	61	7800	
Orion A	0.47	0.13	50.	3.0	2.1×10^4	1.4×10^{-4}	1.7×10^5	340	9200	12;5;13;14
Orion (HII)		0.77	35.	60.	1.5×10^5	4.0×10^{-4}	5.1×10^4	320	6800	
Orion (GMC)		7.4	3.8	500.	3.0×10^5	1.7×10^{-3}	≲1000	130	1800	
NGC 2023	0.48	0.13	11.	0.69	3.9×10^2	1.8×10^{-3}	3.1×10^3	95	7200	11;15;16;17
		0.64	8.0	7.0	2.2×10^3	3.2×10^{-3}	1.0×10^3	73	6800	
NGC 2024 (13')	0.48	0.84	17.	30.	4.0×10^4	7.5×10^{-4}	1.1×10^4	170	6600	18;19;3;20
		1.9	8.5	75.	4.0×10^4	1.9×10^{-3}	2.6×10^3	100	5300	
B35	0.4	0.11	<0.3	<0.01	2.1	$<6.\times10^{-3}$	~24	20	<900	11;21
Carinae I	2.0	0.53	20.	22.	9.0×10^3	2.4×10^{-3}	4.1×10^3	...	...	22;23
G333.6-0.2	4.0	1.17	54.	235.	1.7×10^6	1.4×10^{-4}	2.0×10^5	...	...	11;22;24;27
		4.7	21.	1100.	3.3×10^6	3.5×10^{-4}	3.0×10^4	142	9200	
Sgr A	10.0	2.9	8.4	460.	2.3×10^6	2.0×10^{-4}	4.2×10^4	220	2400	25;26;27
+50/+20 kms^{-1} Clouds	10.0	2.9	9.(+50)	250.	1.6×10^5	1.6×10^{-3}	2.9×10^3	450	1250	28;26;29
			<3.(+20)	<22.	$<2.\times10^5$	$<1\times10^{-4}$	$<3.\times10^3$	540	<340	
Radio Arc	10.0	2.9	12.	330.	7.4×10^5	4.5×10^{-4}	1.4×10^4	270	2800	28;26;30
$\ell^{II}=2.2°$ & 7.3°	10.0	16.0	10.	6400.	1.7×10^6	3.8×10^{-3}	1.3×10^3	340	1900	31;31;32
M17	2.2	0.59	35.	46.	2.3×10^5	2.0×10^{-4}	8.7×10^4	300	7300	33;34;35;32
M17 (HII)		3.9	25.	920.	2.0×10^6	4.6×10^{-4}	2.7×10^4	210	7400	
M17 (GMC)		32.	2.0	8400.	6.0×10^6	1.4×10^{-3}	≲800	68	1800	
W49N	14.	8.2	28.	4700.	6.0×10^6	1.4×10^{-3}	1.8×10^4	310	5700	36;37;38
W51	7.0	1.9	21.	280.	3.2×10^6	8.7×10^{-5}	1.2×10^5	420	3100	36;7;39
		8.2	8.4	1800.	1.3×10^7	1.4×10^{-4}	2.1×10^4	290	1800	4;40;39
W51 (GMC)		19.	3.5	3200.	1.3×10^7	2.5×10^{-4}	≲7×10^3	210	1000	
DR 21	3.0	0.87	17.	42.	1.5×10^5	2.8×10^{-4}	3.1×10^4	300	3500	11;7;37;41
NGC 7023	0.43	0.12	8.5	0.43	4.5×10^2	9.6×10^{-4}	4.5×10^3	39	14000	42;43;44
NGC 7027	1.1	0.32	3.8	1.25	9.0×10^3	1.4×10^{-4}	1.4×10^4	40	5900	45;46;47

^{a} L_{FIR} ≡ far-infrared luminosity of the source in the given beam.

^{b} χ_{FIR} ≡ $L_{FIR}/4\pi D^2\Omega$ (2.0×10^{-4} ergs s^{-1} cm^{-2} sr^{-1}), where D is the source-Earth distance, and Ω is the beam solid angle.

^{c} I_{CO}^* ≡ ∫ $T_R^* dV$ (K km s^{-1}).

REFERENCES.—(1) Howe et al. 1990; (2) Werner et al. 1980; (3) Loren et al. 1981; (4) Melnick et al. 1986; (5) Harper 1974; (6) Brackman & Scoville 1980; (7) Thronson & Harper 1979; (8) Ulich & Haas 1976; (9) Makinen et al. 1985; (10) Kutner et al. 1985; (11) Crawford et al. 1985; (12) Russell et al. 1980; Stacey et al. 1991; (13) Werner et al. 1976; Low & Aumann 1970; Fazio et al. 1974; (14) Schloerb & Loren 1982; (15) Jaffe et al. 1990; (16) Emerson, Furniss, & Jennings 1975; Harvey, Thronson, & Gatley 1980; (17) Milman et al. 1975; (18) Kurtz et al. 1983; (19) Thronson et al. 1984; (20) Tucker, Kutner, & Thaddeus 1973; (21) Lada et al. 1981; (22) Storey et al. 1991b; (23) Harvey, Hoffmann, & Campbell 1979; (24) Hyland et al. 1980; Gillespie et al. 1977; (25) (Δl, Δb) = ($-30''$, 0)($-165 \le v_{LSR} \le -12$ km s^{-1}) Lugten et al. 1986a; (26) Gatley et al. 1977; 1978; (27) Liszt et al. 1983; (28) ($10 \le v_{LSR} \le 70$ km s^{-1}) Genzel et al. 1990; Poglitsch et al. 1991b; (29) Liszt, Burton, & van de Hulst 1985; (30) ($-70 \le v_{LSR} \le -10$ km s^{-1}) Serabyn & Güsten 1987; (31) Stacey et al. 1985; Stacey 1985; (32) Sanders et al. 1986; (33) Russell et al. 1981; Stutzki et al. 1988; Matsuhara et al. 1989; (34) Wilson et al. 1979; Harper et al. 1976; Gatley et al. 1979; (35) Thronson and Lada 1983; (36) Geis et al. 1991; (37) Harvey, Campbell, & Hoffmann 1977; (38) Mufson & Liszt 1977; (39) Mufson & Liszt 1979; (40) Rengarajan et al. 1984; (41) Dickel, Dickel, & Wilson 1978; (42) Chokshi et al. 1988; (43) Whitcomb et al. 1981; (44) Watt et al. 1986; (45) Ellis & Werner 1991; (46) Moseley 1980; Telesco & Harper 1977; (47) Mufson, Lyon, & Marionni 1975.

shown are the predicted [C II] line intensities (in the infinite temperature limit) for these atomic column densities as a function of density for the atomic gas (slanted lines). We have included representative curves for "standard" atomic clouds ($n_H \sim 30$ cm^{-3}, $T_{gas} \sim 100$ K), and the intercloud medium ($n_H \sim 0.10$ cm^{-3}, $T_{gas} \sim 1000$ K). The interpretation of Figure 16 is clear. The observed [C II] line emission from our galaxy sample cannot arise from the "standard" atomic clouds or the intercloud medium because these components do not have the required volume or column densities.

Our new data reinforces an important conclusion of CGTW and extends it to include a wide variety of Hubble types, star formation rates, and luminosity class in galaxies: *the bulk of the measured* [C II] *line radiation does not arise in the "standard" atomic gas clouds or the intercloud medium*—if the observed 21 cm line emission arises from such regions, then the 21 cm and
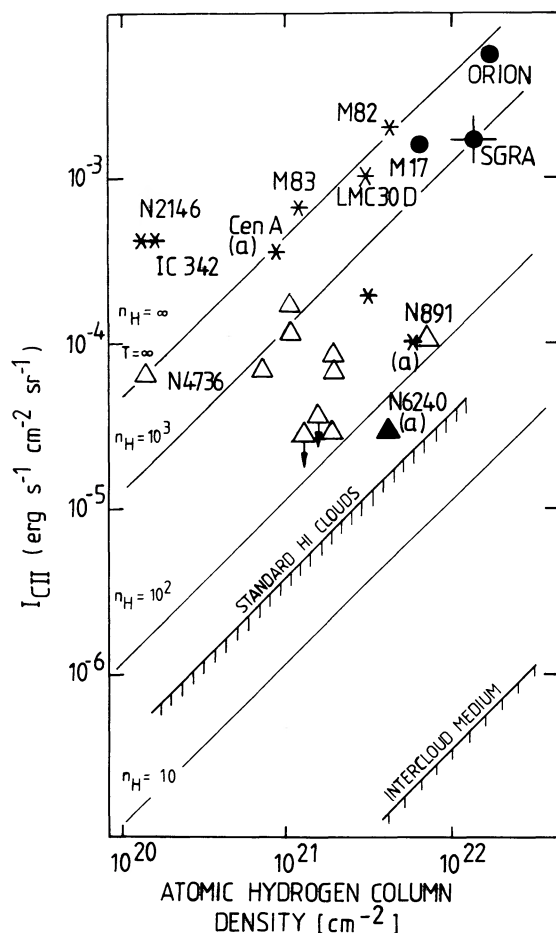
FIG. 16.—Integrated [C II] line intensity as a function of atomic hydrogen column density derived from 21 cm H I measurements.' Lines of 45° slope represent calculated [C II] line intensities for the indicated volume densities in the infinite temperature ($T \gg 91$ K) limit. The locations of "standard" H I clouds ($n_H \sim 30$ cm^{-3}, $T_{kin} \sim 100$ K) and of the H I intercloud medium ($n_H \sim 0.1$ cm^{-3}, $T_{kin} \sim 1000$ K) are also indicated.

[C II] lines must largely trace different components of the interstellar medium. Also, the [C II] line emission is too bright to be consistent with emission from compact H II regions or from extended low-density H II regions (Stacey et al. 1985; Stacey 1985; CGTW).

4.5. Comparison with the Far-Infrared Continuum

In the high-extinction environments of the nuclear regions of gas-rich galaxies, most of the emitted UV flux from early-type stars will be absorbed by nearby dust grains which then reradiate the energy in the FIR. Thus, the FIR continuum intensity, χ_{FIR}, is related to the UV field intensity, χ_{UV}, in a linear manner ($\chi_{UV} \sim \chi_{FIR}$). Here χ_{UV} is defined as the interstellar far-UV radiation field ($6.2 \leq h\nu \leq 13.6$ eV) in units of the local interstellar radiation field ($\chi_0 = 2.0 \times 10^{-4}$ ergs s^{-1} cm^{-2} sr^{-1}; Draine 1978).

There is a good correlation between the FIR continuum intensity, χ_{FIR} (Table 3, col. [10]) and the [C II] line intensity (Fig. 17). This correlation, however, is significantly nonlinear indicating that the increase in the [C II] line with the FIR continuum intensity is not simply due to an increase in the number of [C II] and FIR-emitting clouds (mass) in the beam. The [C II] line-to-FIR continuum ratio decreases as the FIR

intensity increases. This implies that the efficiency with which ultraviolet radiation is converted into [C II] emission *decreases* as the UV field intensity *increases*—therefore, for sources with the higher (inferred) UV fields, there must be less efficient conversion of this UV energy into [C II] line radiation.

5. DISCUSSION

The good spatial and spectral correlation between the [C II] and ^{12}CO ($1 \rightarrow 0$) line radiation in a wide variety of Galactic and extragalactic regions demonstrates that the [C II] radiation originates from the immediate vicinity of dense molecular clouds. The data presented here confirm that on a galactic scale the observed [C II] radiation, in both starburst and normal spiral galaxies, is best explained as arising in the warm ($T > 200$ K), dense ($n_H > 10^3$ cm^{-3}) photodissociation regions at the surfaces of giant molecular clouds.

5.1. The [C II], ^{12}CO ($1 \rightarrow 0$), χ_{FIR} Correlation

5.1.1. The Link between the Galactic and Extragalactic Interstellar Medium

The ^{12}CO ($1 \rightarrow 0$) line emission from galaxies is usually presumed to be dominated by the emission from the cold disk molecular component and to therefore trace molecular mass in external galaxies (cf. § 5.2 below; CGTW). These cold molecular clouds should produce relatively little [C II] line radiation because of the low ambient UV fields. This conclusion is supported observationally by [C II] cuts taken across the Orion and M17 molecular clouds (Stacey et al. 1991; Stutzki et al. 1988; Matsuhara et al. 1989). In the high UV ($\chi_{FIR} \sim 10^5$) photodissociation region associated with the H II region/GMC region interface, the integrated [C II]/^{12}CO ($1 \rightarrow 0$) line intensity ratio is ~ 7100. However, over the bulk of the M17 SW and Orion molecular clouds, where the UV fields are much weaker ($\chi_{FIR} < 1000$), this ratio is factors of 3–4 smaller (Table 5, col. [10]; Fig. 15b). The case is similar for the W51 molecular cloud (Table 5; Melnick et al. 1986; Geis et al. 1991) and the non–OB star-forming $+20$ and $+50$ clouds near the Galactic center (Table 5; Genzel et al. 1990). Stacey et al. (1985) (see also Shibai et al. 1991) have measured the [C II] intensity from cuts across the plane of the Galaxy through regions specifically chosen to avoid outward signs of star formation ($l = 2°2$ and $7°3$). These measurements indicate that *integrated over the Galaxy*, the [C II]/^{12}CO ($1 \rightarrow 0$) ratio is significantly smaller (<2000) than in Galactic OB star formation regions.

We may therefore expect that if a substantial fraction of the ^{12}CO ($1 \rightarrow 0$) emission from galaxies were originating from such cold disk molecular clouds the [C II]/CO line intensity ratio would be substantially less than what we observe in Galactic OB star formation regions. We may also expect this ratio to vary significantly depending on just how the UV energy is distributed. This is exactly what we find for the non-starburst galaxies in our sample: the [C II]/^{12}CO ($1 \rightarrow 0$) line intensity ratio does vary from galaxy to galaxy and is always less than the ratio observed in Galactic OB star formation regions. This suggests that the [C II] and ^{12}CO ($1 \rightarrow 0$) line emission from these galaxies arises from the surfaces of molecular clouds exposed to small UV fields—similar to the molecular clouds found in the Galactic disk. On the other hand, the line intensity ratio in the nuclear regions of the starburst galaxies is a near constant value, closely equal to the value of this ratio in Galactic OB star formation regions. This suggests that the physical conditions in the emitting gas of Galactic OB star
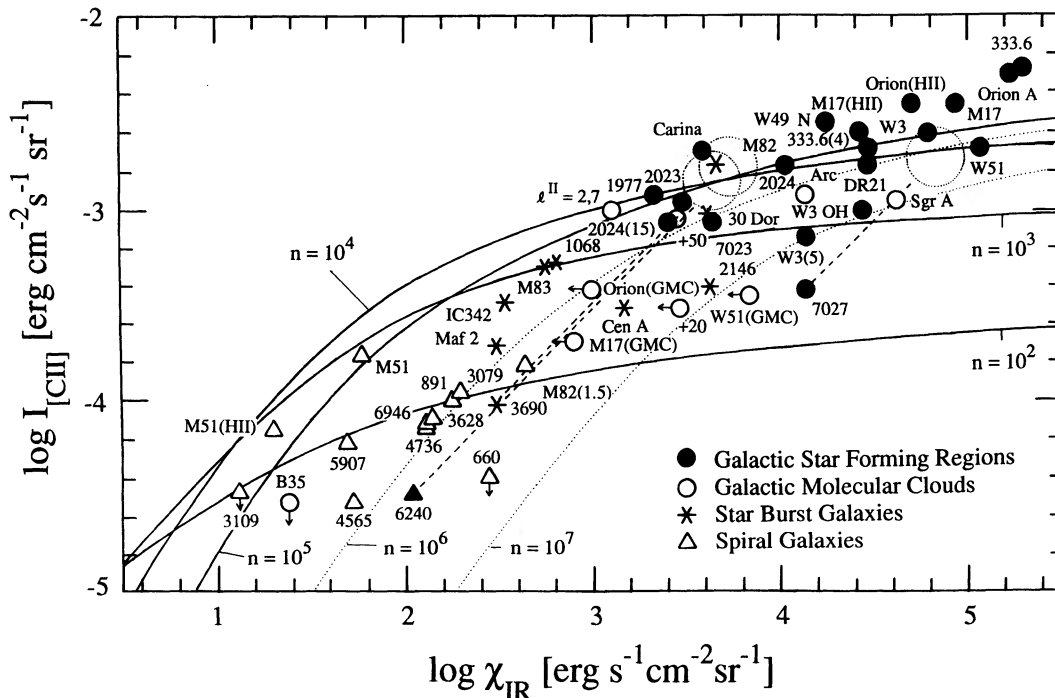
FIG. 17.—Correlation between the [C II] line intensity of Galactic and extragalactic regions and the FIR intensity χ_{FIR} (in units of 2.0×10^{-4} ergs s^{-1} cm^{-2} sr^{-1}). We have superposed the calculated [C II] flux expected for a cloud densities between 10^2 and 10^6 cm^{-3} for the FIR continuum intensities. Corrections for those sources with [C II] and FIR filling factors significantly less than unity are indicated by dashed arrows to the upper left on the figure. The filling factors for NGC 3690/IC 694 and NGC 6240 are estimated from the work of Joy et al. (1989) and Rieke et al. (1985), respectively.

formation regions and the nuclear regions of starburst galaxies are similar. It is easily demonstrated, however, that the observed [C II] and ^{12}CO (1 → 0) line radiation from galaxies is *not* produced in a simple superposition of Orion-like H II regions.

In the high UV ($\chi_{UV} > 10^4$) field environments of the photodissociation regions associated with Orion-like H II regions, the observed [C II] line-to–FIR continuum ratio is small ~ few × 10^{-4} (Table 5, col. [7]). However, in *all* of the observed galaxies, including those with starburst nuclei, the [C II] line-to–continuum ratio is much larger, ~ few × 10^{-3} (Table 3, col. [9]). Therefore, even if *all* of the observed FIR continuum were to originate in Orion-like star formation regions, the [C II] flux from such regions would fail by an order of magnitude to account for the observed [C II] flux. These regions cannot be the sole source (or even the dominant source) of [C II] flux for any of the program galaxies.

5.1.2. The Molecular Medium in Starburst Galaxies

The observed [C II]/CO line intensity and [C II]/FIR continuum intensity ratios in starburst galaxies are inconsistent *both* with Galactic GMCs or Orion-like star formation regions. The line ratios are, however, consistent with the ratios found for the moderate UV field ($\chi_{UV} \sim 10^3$), Galactic sources in our sample, e.g., NGC 1977 and NGC 2023. These sources are excited by early B stars and have inferred UV fields somewhere between those found in Galactic OB star formation regions ($\chi_{UV} \sim 10^4$–10^5) and Galactic GMCs ($\chi_{UV} < 10^3$)—fields which are consistent with the inferred UV fields for the starburst galaxies. If the *bulk* of the molecular medium in starburst galaxies were exposed to elevated ($\chi_{UV} \sim 10^3$) UV radiation fields, this medium would reproduce the observed

line and continuum ratios. We therefore expect that the average molecular medium in starburst galaxies is intermediate in excitation between the low-UV exposed GMCs in normal spiral galaxies and the high-UV exposed GMCs gas found in the environments near Galactic star formation regions.

5.1.3. Excitation Conditions of the CO-emitting Gas

The high-UV fields associated with Galactic OB star formation regions have a very large effect on the excitation of the molecular gas. In Orion, for example, the CO-emitting gas interior to the photodissociation regions is demonstrated to be warm ($T_{gas} > 100$ K) both through the high brightness temperatures obtained in the ^{12}CO (1 → 0) line ($T_b \approx 100$ K; Schloerb & Loren 1982) and through the existence of bright high-J ($J = 7 \rightarrow 6$; 14 → 13) CO rotational emission (Schmid-Burgk et al. 1989; Stacey et al. 1991), from the interface region. There is also evidence for warm molecular gas at the interface regions in M17 and NGC 2023 (Harris et al. 1987; Jaffe et al. 1990). We therefore conclude that the molecular gas in the nuclei of starburst galaxies may be similarly affected by the high UV fields in the nuclei.

There is direct observational evidence for this effect. Lo et al. (1987) have constructed high spatial resolution interferometer maps of the ^{12}CO (1 → 0) transition of the central regions of M82. The measured antenna temperatures of the clumps in their maps are consistent with gas excitation temperatures of about 40 K. Wild et al. (1991) arrive at a similar conclusion through a multilevel (up to $J = 6 \rightarrow 5$) study of the CO emission from this galaxy. The situation is similar for the central regions of IC 342 (Eckart et al. 1990) The CO line emission from starburst galaxies may therefore be tracing a combination of gas excitation and mass. The Galactic ^{12}CO (1 → 0) line

intensity–to–molecular mass conversion ratio may therefore be somewhat inappropriate for the high-UV environments of these starburst galaxies. This conclusion has important implications for the star formation efficiency inferred by the ^{12}CO $(1 \to 0)$ gas mass estimates.

5.2. Mass of the Photodissociated Gas

The mass contained in photodissociation regions may be a substantial fraction of the total gas mass in a galaxy. In Table 3, column (6), we tabulate the minimum column density of singly ionized carbon ions required to give the observed [C II] line intensity from each of the observed sources. This column density is calculated for the high temperature ($T \gg 91.4$ K), high-density ($n_H \gg 2 \times 10^3$ cm^{-3}) limit. The actual column densities may be larger by factors of order 2–5. For the galaxies for which [O I] (63 μm) radiation has been reported (M82, IC 342, NGC 3690, and NGC 6946; Watson et al. 1984, Lugten et al. 1986b, Duffy et al. 1987, Genzel & Stacey 1985, Eckart et al. 1990, Lord et al. 1991) the measured [O I] to [C II] line ratio (which is sensitive to gas pressure) indicates C$^+$ column densities roughly twice the numbers reported in Table 3. Column (7) tabulates the minimum column of hydrogenic nuclei corresponding to this C$^+$ column under the assumption [C$^+$]/[H] = 3 × 10^{-4}.

Table 4, column (5) lists the column density of molecular hydrogen estimated for each galaxy if one uses the conversion factor between integrated ^{12}CO $(1 \to 0)$ line emission and N_{H_2} determined for cold disk clouds in the Galaxy ($N_{H_2} \sim 3 \times 10^{20} I^*_{CO}$ [K km s^{-1}]; Bloemen 1989). This conversion factor is based on three assumptions: (1) the CO-emitting clouds are optically thick in the ^{12}CO $(1 \to 0)$ line (so that the brightness of the CO line is a measure of the filling factor of clouds in the beam); (2) all clouds have about the same CO gas excitation temperature ($T_{ex} \simeq 10$ K) and density distribution; and (3) the CO line width scales as the cloud mass according to the virial theorem (CGWT, Appendix B). If this is the correct conversion ratio, then the minimum hydrogen mass in photodissociation regions (inferred from the observed minimum C$^+$ column) is a small (1%–10%) fraction of the molecular gas mass. If, however, the ^{12}CO $(1 \to 0)$ line emission in IR-luminous galaxies is produced in warm ($T_{ex} \gtrsim 40$ K) molecular gas, as suggested in § 5.1.3 above, then the inferred molecular hydrogen column density may be up to an order of magnitude smaller (Table 4, col. [4]). The gas mass contained in photodissociation regions for the IR-bright galaxies is then comparable (up to ~70%) to the molecular gas mass.

A comparison with the observed 21 cm line emission leads to a similar result. In Table 4, column (10) we tabulate the ratio of the minimum column density of hydrogenic nuclei in photodissociation regions to the atomic column density as traced through its 21 cm line (col. [8]). For most of the quiescent galaxies, this ratio is small ~4%–25%. However, for the starburst galaxies, this ratio is much larger, in some cases exceeding unity. The photodissociated gas mass for these starburst nuclei may therefore *exceed* the atomic gas mass.

Table 4, column (11) tabulates the minimum gas mass contained in the photodissociation regions. For most of the galaxy sample, the required photodissociated gas mass is substantial, exceeding 10^7 $M_\odot$ in the nuclear regions. The photodissociated mass fraction (col. [12]) for the quiescent spiral galaxies ranges from 3% to 15% of the total gas mass, in good agreement with the photodissociated gas fraction obtained for our own Galaxy (~4% to 8%; Stacey 1985). For several of the IR-bright gal-

axies (e.g., NGC 1068, NGC 2146, and NGC 3690) the photodissociated gas mass in the nuclear regions exceeds 10^8 $M_\odot$. Photodissociated gas therefore represents a substantial fraction (up to 40%) of the total gas mass in the galactic nuclei and may be *the dominant phase of the interstellar medium* in starburst nuclei.

5.3. Theoretical Interpretation

5.3.1. Correlation with the FIR Continuum

We have computed the [C II] 158 μm and ^{12}CO $(1 \to 0)$ line emission that is expected to be produced in the photodissociation gas regions at the surfaces of molecular clouds exposed to far-ultraviolet radiation fields. The calculations were performed using models similar to those presented by Tielens & Hollenbach (1985) and Sternberg & Dalgarno (1989). We assumed undepleted gas-phase fractional abundances of carbon and oxygen equal to 3 × 10^{-4} and 6 × 10^{-4}, respectively, and that the far-UV dust opacity is equal to $1.8 A_V$. The gas chemistry and thermal balance are computed as functions of cloud depth in a plane parallel geometry and proceed from the cloud surface to regions deep within the molecular cloud where the incident far-UV radiation is fully absorbed ($A_V > 10$). Radiative transfer in optically thick emission lines is approximated using an escape probability formalism.

The theoretically predicted [C II] line intensities are presented as functions of the UV intensity (which is parameterized by χ_{FIR}) for various values of the hydrogen gas density, n_H in Figure 17. At a given value of n_H the [C II] intensity effectively saturates at large values of χ_{FIR} because for such radiation field intensities the total column density of [C II] is determined by the dust penetration depth of the UV photons which varies only logarithmically with χ_{FIR}. For smaller UV field intensities, the [C II] intensity decreases rapidly with decreasing χ_{FIR} because the [C II] column density is then determined by the [C II] formation rate which is proportional to the UV field intensity, and because as the UV field decreases, a decreasing fraction of the [C II] emitting gas is at a temperature which is above the transition temperature (92 K) of the 158 μm line.

Those sources which fall significantly below the saturation curve, may have less [C II] line radiation per unit UV field strength for several reasons. For some sources the UV fields may be significantly larger than the value in column (10) of Table 3 due to beam filling factor effects. This is clearly the case for sources such as the distant galaxies NGC 3690 and NGC 6240, and for the planetary nebula NGC 7027. For sources which do not fill the beam, the UV field and the [C II] line intensity would both be underestimated by the same amount. We may correct for this effect in those sources for which the beam filling factor is known or can be estimated from other data. These corrections are indicated with dashed arrows to the upper right on Figure 17. Cloud density variations from galaxy to galaxy, or a nonuniform distribution of the UV field strength within a galaxy could also result in a lowered [C II] line emission per unit UV flux.

A few sources actually fall somewhat above the maximum predicted [C II] line intensities of the PDR models (e.g., M42). Enhanced [C II] emission may arise from geometric effects. The model calculations predict the [C II] emission-line intensity along a direction which is normal to the cloud surface. If the line of sight to the surface is inclined relative to the normal, the observed column density of [C II] is increased and so is the intensity of the optically thin [C II] line. Similarly, if the UV

source is embedded in a molecular cloud, the observed [C II] emission may arise from both the near and far walls of the cavity thereby increasing the amount of [C II] emission produced for a given amount of ultraviolet radiation. The [C II] emission may also be enhanced in sources where the effective grain UV absorption cross section per hydrogen nucleus is smaller than assumed in the calculations because of a small dust abundance or because of unusual dust UV scattering properties.

5.3.2. Estimates of χ_{UV}, and n_H, and Φ

There is a noticeable trend in the starburst galaxies data for the brighter [C II] line intensities to be associated with the more nearby galaxies. For example, the [C II] line is brightest in the nearby starburst galaxy M82 ($D = 3.3$ Mpc, $I_{[C II]} = 1.5 \times 10^{-3}$ ergs s^{-1} cm^{-2} sr^{-1}) substantially weaker for NGC 2146 ($D = 14.4$ Mpc, $I_{[C II]} = 3.9 \times 10^{-4}$ ergs s^{-1} cm^{-2} sr^{-1}) and weakest in the distant interacting $IRAS$ galaxy, NGC 3690/IC 694 ($D = 44$ Mpc, $I_{[C II]} = 9.4 \times 10^{-5}$ ergs s^{-1} cm^{-2} sr^{-1}). This suggests that the measured variations in absolute line intensity for these starburst galaxies is largely a source beam filling factor effect.

Wolfire, Hollenbach, & Tielens (1989) have suggested a technique for eliminating the contribution that the beam filling factor makes to the observed [C II]/^{12}CO (1 → 0) correlation. If it is assumed that the [C II], ^{12}CO (1 → 0) line and FIR continuum emission are associated with the same photodissociation regions the ratios $Y_{[C II]} \equiv I_{[C II]}/\chi_{FIR}$ and $Y_{CO} \equiv I_{CO}/\chi_{FIR}$ are independent of the beam filling factor Φ. The observed values of $Y_{[C II]}$ and Y_{CO} are plotted in Figure 18 in the $Y_{[C II]}$-Y_{CO} plane along with theoretically computed contours of

constant gas density, n_H, and UV intensity, χ_{UV} (where the beam filling factor $\Phi \equiv \chi_{FIR}/\chi_{UV}$). The theoretical curves may be understood by noting that at fixed density (solid curves) $Y_{[C II]}$ is an increasing function of Y_{CO} when χ_{UV} is sufficiently large because both the [C II] and CO line intensities are then roughly independent of the UV field. For sufficiently small values of χ_{UV}, however, $Y_{[C II]}$ decreases as Y_{CO} increases (at fixed density) because the [C II] line intensity decreases rapidly with decreasing χ_{UV} while the CO intensity is insensitive to χ_{UV}. At a fixed UV field intensity (dashed curves) $Y_{[C II]}$ increases with the gas density when $n_H < n_{crit}([C II])$, where $n_{crit}([C II])$ is the critical density of the [C II] fine-structure transition ($\sim 3 \times 10^3$ cm^{-3}). At larger values of the density, $N_{[C II]}$ is proportional to the dust penetration depth which increases only logarithmically with χ_{UV}, thus the ratio $Y_{[C II]}$ decreases slowly. $Y_{[C II]}$ decreases rapidly at still higher densities where $N_{[C II]}$ is proportional to the [C II] formation rate. On the other hand, Y_{CO} (and I_{CO}) increase with n_H when $n_H < n_{crit}(CO)$, where $n_{crit}(CO)$ is the critical density of the CO (1 → 0) transition ($\sim 3 \times 10^3$ cm^{-3}) but are insensitive to the density at larger values of n_H. Therefore, the constant χ_{UV} contours in Figure 18 slope up and to the right when χ_{UV}/n_H is large, but drop almost vertically when χ_{UV}/n_H is small (<0.01). Almost all of the observed sources lie within the region of the Y_{CO}-$Y_{[C II]}$ plane with 10^2 cm$^{-3} < n_H < 10^7$ cm^{-3} and $10 < \chi_{UV} < 10^5$. Any point within this region is consistent with a particular range of possible densities and UV field intensities rather than a unique value of χ_{UV} and n_H. However, the possible range of values of n_H and χ_{UV} for the various sources may be inferred using Figure 18. The inferred densities for nearly all of the galaxy sample lie
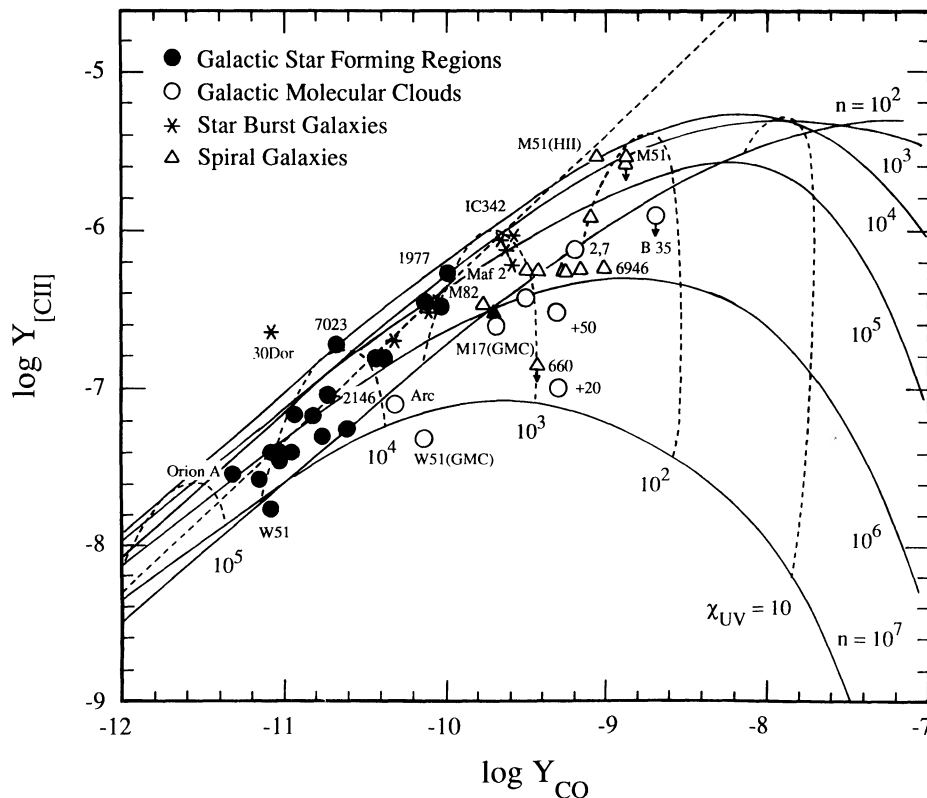

FIG. 18.—$Y([C II])$ vs. $Y(CO)$ for the observed sources. We have superposed the predictions of the photodissociation model as a function of n_H and χ_{UV}. The dashed line indicates the [C II]/^{12}CO (1 → 0) line intensity ratio observed for starburst galaxies and galactic OB star formation regions (6300).

between 10^3 and 10^6 cm^{-3}. For the Galactic OB star forma-
tion regions the inferred UV field intensity is large, with $10^4 <$
$\chi_{UV} < 10^5$. For the starburst galaxies $10^3 < \chi_{UV} < 10^4$, and for
the nonstarburst galaxies and Galactic molecular clouds,
$\chi_{UV} < 10^3$. Thus the theory supports our observational evi-
dence that the UV fields in the starburst galaxies must lie
midway between those found in Galactic OB star formation
regions and those found in Galactic disk molecular clouds.

For both Galactic and extragalactic sources, $\chi_{UV} \sim \chi_{FIR}$, so
the beam filling factors, Φ, for the [C II]–emitting gas are near
unity (Table 3, col. [11]). The beam filling factor is the product
of the area filling factor and the velocity filling factor—both of
which may exceed unity for the optically thin [C II] line.
Typical filling factors for the program galaxies are ~0.3, the
notable exceptions being M82, for which $\Phi > 1$, and the
distant IR-bright galaxies NGC 3690 and NGC 6240 for which
$\Phi \sim 0.05$.

5.3.3. The [C II]/^{12}CO (1 → 0) Correlation

The average [C II]/^{12}CO (1 → 0) line intensity ratio for the
starburst galaxies and Galactic OB star formation regions
($I_{[C II]}/I^*_{CO} \sim 6300$) is indicated by a dashed line to the upper
right in Figure 18. A ratio of 6300 occurs for any region where
the UV field is greater than ~10^3, and χ_{UV}/n_H is near unity (see
also Wolfire et al. 1989). Since molecular cloud densities are
typically 10^3 cm^{-3}, then the observed ratio is theoretically
expected for high UV field strengths (> 10^3).

5.3.4. 21 Centimeter Line Emission and Photodissociation Regions

We have demonstrated above that the [C II] line emission
from galaxies does not arise in "standard" atomic clouds or

the diffuse interstellar medium (traced by the H I 21 cm line).
However, the converse is not true. A large fraction of the
observed 21 cm line emission from the nuclei of IR-bright
galaxies may, in fact, arise from the warm, *dense* photo-
dissociation regions traced by their [C II] line emission. The
H I column density in a given photodissociation region
depends on the ratio between the impinging UV field strength,
χ_{UV} and the molecular cloud density, n_H (Sternberg 1988):

$$N_{HI} = 5 \times 10^{20} \ln(90\chi_{UV}/n_H + 1) \text{ cm}^{-2} .$$

Figure 19 plots the calculated contours of constant N_{HI} in the
Y_{CO}-$Y_{[C II]}$ plane. For the galaxy sample, typical values of χ_{UV}
and n_H are $10^2 < \chi_{UV} < 10^4$; $10^2 < n_H < 10^4$. The inferred
column densities of atomic hydrogen in the photodissociation
regions, $N_{HI(PDR)}$, are therefore between 3 and 46 $\times 10^{20}$ cm^{-2}.
The atomic column density in our [C II] beam is related to
that in the PDR by the beam filling factor, Φ. For most gal-
axies, $\Phi \sim 0.3$ so that typical beam-averaged column densities
of atomic hydrogen in the PDR are ~1 to 14 $\times 10^{20}$ cm^{-2}.
Therefore, the atomic gas column in the PDR is always a
substantial fraction of the total hydrogen gas column in the
PDR (Table 3, col. [7]). Previous theoretical models estimate
this fraction to be 30%–50% (Jura 1978; Tielens & Hollenbach
1985). If we take a typical fraction to be 40%, then, for the
more quiescent normal spiral galaxies, e.g., NGC 891 and
NGC 6946, the ratio of atomic hydrogen inferred to be in
PDRs to the total observed H I column density is about
2%–10% (Table 4, col. [10]). For the IR-bright galaxies M82,
M83, and Cen A, however, this fraction is significantly
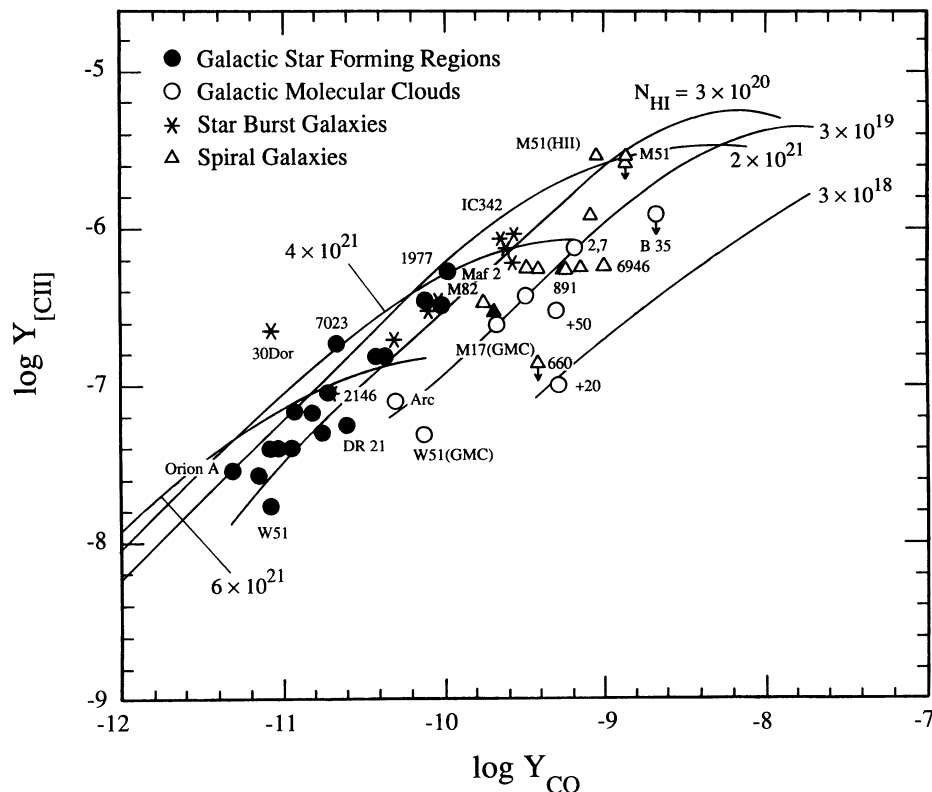higher—approaching 50%. An extreme example is the star-

FIG. 19.—$Y([C II])$ vs. $Y(CO)$ for the observed sources. We have superposed the predictions of our photodissociation region model for the column density of
atomic hydrogen in the PDR, $N_{HI(PDR)}$.

burst galaxy IC 342 for which the *minimum* atomic column density in PDRs is *twice* the atomic column density traced through its 21 cm emission. The beam for the 21 cm measurement is somewhat larger (2′ vs. 55″) than our [C II] beam, so beam dilution may have a significant effect on the 21 cm estimate. However, it is clear that a substantial fraction of the 21 cm line emission from the nuclear regions of IC 342 arises from warm ($T_{gas} \geq 200$ K), dense ($n_H \geq 10^3$ cm^{-3}) [C II] emitting photodissociation regions associated with molecular clouds and not from low-excitation ($T_{gas} \sim 80$ K; $n_{H I} \sim 10-10^3$ cm^{-3}) atomic gas clouds as is commonly assumed (cf. Kulkarni & Heiles 1988).

Tilanus & Allen (1989) have recently obtained a high spatial resolution interferometric map of M51 in the H I 21 cm line. Comparison of the H I map to other tracers of spiral structure reveals that the atomic gas is coincident with the Galactic H II regions (as traced by their Hα emission) but significantly displaced toward larger Galactic radii with respect to the regions of maximum compression of the interstellar gas (traced by the nonthermal radio continuum emission) and the spiral dust lanes (which follow the nonthermal radio continuum). On the other hand, the ^{12}CO (1 → 0) aperture synthesis maps obtained by Vogel, Kulkarni, & Scoville 1988 indicate that the molecular gas *is* coincident with the spiral dust lanes. Since the atomic gas is downstream of the spiral dust lanes and molecular gas, Tilanus & Allen conclude that the H I ridges are largely the result of the photodissociation of molecular clouds by the UV starlight of nearby OB stars. Much of the atomic medium in this galaxy is therefore the product—not the precursor—of star formation activity. A similar conclusion is attained for M83 (Allen, Atherton, & Tilanus 1986). This important result is consistent with our conclusions above: a significant fraction of the observed atomic column in star-forming galaxies may be the result of the photodissociation of molecular clouds by the early-type stars. This photodissociated atomic gas is then manifest as the atomic medium "downstream" of the sites of star formation activity.

5.4. [C II], χ_{FIR}, ^{12}CO (1 → 0) *and Star Formation Activity*

Because the [C II] line is very sensitive to the local UV energy density in regions of low field strength, the relative intensity of this line may be used as a sensitive probe of OB star formation activity in galaxies. The [C II] line has an advantage over other infrared lines which may trace star formation such as the [O I] 63 μm and 145 μm and the near-IR molecular hydrogen rovibrational lines in that [C II] emission is thought not to be significantly excited in shocks (Hollenbach & McKee 1989). The [C II] 158 μm to ^{12}CO (1 → 0) line intensity ratio is a particularly useful quantity as taking the ratio largely removes the effects of filling factors. Figure 20 (*top*) displays the ^{12}CO (1 → 0) (*left*) and [C II] 158 μm (*right*) spectra obtained for the central regions of the infrared-bright galaxy NGC 2146. The bottom panel displays the same two lines toward the quiescent Sbc spiral galaxy, NGC 3628. We scale both the CO and [C II] spectra for NGC 2146 by a factor of 1.5 so that the peak CO antennae temperatures for the two galaxies are identical. The dramatic effects of the large star formation activity in NGC 2146 are apparent. While the ^{12}CO (1 → 0) lines for both galaxies are comparable, and the FIR flux differs by less than a factor of 3, the [C II] 158 μm line emission is nearly *10 times* weaker in the "normal" spiral galaxy NGC 3628. The observed ^{12}CO (1 → 0) emission from NGC 3628 is therefore dominated by emission from cold molecular gas
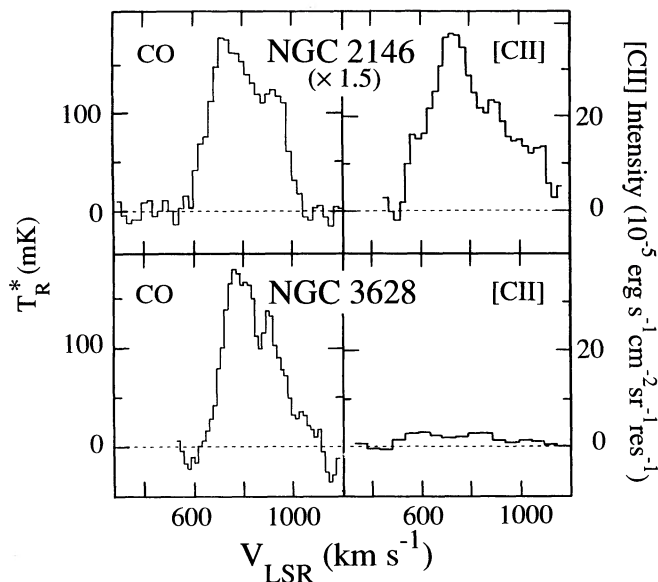

FIG. 20.—Comparison between the [C II] and ^{12}CO fluxes from NGC 2146 (*top*) and NGC 3628 (*bottom*). While both the galaxies have similar CO line intensities (*left*), the [C II] line is 10 times brighter in the starburst galaxy NGC 2146 than in the quiescent spiral galaxy NGC 3628, consistent with large amounts of star formation activity in NGC 2146.

associated with small (normal) amounts of star formation activity. For NGC 2146, the [C II]-to-^{12}CO (1 → 0) line intensity ratio is identical to Galactic OB star formation regions consistent with a large degree of star formation activity in the molecular clouds associated with this galaxy.

The dependence of the [C II]/^{12}CO (1 → 0) line intensity ratio on star formation activity is also illustrated by our mapping of the starburst galaxy M82. In the nuclear regions of the galaxy, the line intensity ratio is high (~ 6100), consistent with the high UV radiation fields ($\chi_{FIR} \sim 4700$) and high rates of star formation activity here. In the regions away from the nuclear starburst ($r = 90'' \Leftrightarrow 1.44$ kpc) the line intensity ratio is much smaller (~ 2500; Table 4, Fig. 14) consistent with much smaller rates of star formation activity, and much smaller UV radiation fields ($\chi_{FIR} \sim 440$) in these extranuclear regions.

Estimates of Galactic star formation activity are also deduced from the observed FIR luminosity of a galaxy assuming that this FIR flux arises largely as reradiated UV flux from nearby OB stars. However, a significant fraction of the FIR luminosity of infrared-luminous galaxies may arise from nonstellar sources, e.g., active galactic nuclei (cf. Rodriguez Espinosa, Rudy, & Jones 1986). These nonstellar sources are presumably confined to the nuclear regions of galaxies, and, as such, have both very intense far-UV fields, and small beam filling factors. Due to the saturation of the [C II] line in such high UV fields, the line-to-continuum ratio will be small for such regions, similar to the line-to-continuum ratio for Galactic OB star formation regions. Therefore, while such regions may dominate the FIR flux, they will contribute little to the [C II] line intensity producing a very low [C II]-to-FIR line intensity ratio. This is analogous to our previous conclusion that a simple superposition of Orion-like H II regions will not reproduce the observed extragalactic [C II]/FIR intensity ratio.

The relative ratios of the [C II] and the ^{12}CO (1 → 0) line and the FIR continuum intensities may therefore be used as a

probe of the degree to which nonstellar activities contribute to the FIR flux. An integrated line ratio of the order 6300 indicates that much of the observed emission in both the [C II] and the ^{12}CO lines arises from an overall neutral interstellar medium which is exposed to elevated UV fields ($\chi_{UV} > 1000$) associated with OB star formation. If, however, a galaxy has both high CO line intensity and a large FIR flux, but small [C II] line emission (e.g. NGC 6240 below), then the observed FIR flux must be concentrated such that it fills a small portion of the FIR, [C II], and ^{12}CO beams. If the FIR flux arises from OB star formation, the star formation regions must be relatively confined.

5.5. Comments on Individual Galaxies

5.5.1. Large Magellanic Cloud

Storey et al. (1991a) mapped the [C II] line intensity over a ~4' region near the 30 Doradus nebula in the LMC. The [C II]–to–^{12}CO (1 → 0) line intensity ratio for this source is the only ratio greatly in excess of the ratio found for OB star formation regions in the Galaxy. The large observed ratio is best understood as an effect of the low abundance of heavy elements in the LMC.

The LMC is underabundant in the heavy elements by a factor of 6 relative to the solar value (Dufour, Shields, & Talbot 1982). Since the penetration depth of carbon ionizing photons into molecular clouds is determined by the absorption of those photons by dust, any decrease in carbon abundance which is accompanied by a decrease in dust abundance will result in the same total column density of C$^+$. Therefore the [C II] line intensity for a metal-poor cloud will be roughly the same as that from a metal-rich cloud. Similarly, for a molecular cloud of large column density, the optically thick ^{12}CO (1 → 0) line intensity will also be relatively unaffected (Kutner & Leung 1985). Therefore, for a single face on PDR, one would expect the integrated line intensity ratio to be largely unaffected by changes in metallicity (Wolfire et al. 1989). However, the CO-emitting "core" of a UV-exposed molecular cloud will be relatively much smaller than the photodissociated "skin" for a low-metalicity cloud. Therefore, photodissociated gas occupies a relatively larger volume of the interstellar medium, resulting in an enhanced [C II]/^{12}CO (1 → 0) line intensity ratio (Maloney & Black 1988). Similarly, the relatively small CO-emitting cores of these molecular clouds result in a much larger CO luminosity to molecular mass conversion factor (Cohen et al. 1988).

5.5.2. NGC 6240

The ultraluminous *IRAS* galaxy NGC 6240 provides an excellent example of the usefulness of the [C II], ^{12}CO (1 → 0), and FIR continuum ratios in discerning the extent of OB star formation activity in a galaxy. The relative smallness of the [C II]/CO line intensity ratio (~2300) by itself indicates that this galaxy is not undergoing a *global* burst of star formation activity. The FIR continuum intensity may then be used to constrain the spatial extent of star formation activity. For a single component model, the observed [C II], ^{12}CO (1 → 0), and FIR continuum flux ratios have two theoretical solutions (Fig. 18). The low-density solution requires moderate density clouds ($n_H \sim 10^2$ cm^{-3}) and moderate UV field strengths ($\chi_{UV} \sim 4 \times 10^2$). The high-density solution requires very high density molecular gas ($n_H \sim 10^6$ cm^{-3}), and higher UV fields ($\chi_{UV} \sim 2 \times 10^3$). However, Rieke et al. (1985) find that most of the *IRAS* 12 flux is confined to the inner 3″ radius (1.5 kpc)

regions of this peculiar galaxy. Assuming the near-infrared and far-infrared fluxes have similar spatial distributions, this means that the average UV fields in the inner regions of NGC 6240 are greater than 10^4, nearly 10 times the maximum theoretical value for a single-component model. Therefore, the large FIR continuum, large CO intensity, and small [C II] line intensity for this galaxy are not well fitted by these single component models. For a good fit, we require instead two components: (1) a high-UV field ($\chi_{UV} \sim 10^4$), small filling factor (comparable in extent to the 12 μm flux) component; and (2) a low-UV field ($\chi_{UV} < 100$), relatively large filling factor component. If we assume both components have densities ~10^3 cm^{-3}, the first component would produce much of the observed FIR continuum, but relatively little of the lines ($I_{[C III]} \sim 10^{-5}$ ergs s^{-1} cm^{-2} sr^{-1}, $I^*_{CO} \sim 1$ K km s^{-1}). The low-UV fields in the second component result in a low [C II]–to–^{12}CO (1 → 0) line intensity ratio, and produce relatively little of the observed FIR continuum. The first component could be a confined region of star formation activity or a dust-enshrouded active galactic nucleus.

6. SUMMARY

We report 158 μm [C II] fine-structure line observations of a sample of 14 gas-rich galaxies. Our new measurements confirm and generalize the basic results of CGTW: The [C II] line is bright amounting to ~0.1%–1% of the far-infrared luminosity of the nuclear regions of galaxies. The [C II] line is formed in the warm ($T_{gas} > 200$ K), dense ($n_H > 10^3$ cm^{-3}) photo-dissociated gas at the interfaces between giant molecular clouds and ionized gas regions and is therefore associated with the *molecular gas* component in spiral galaxies. The [C II] line tracks the FIR continuum in a manner consistent with the PDR models. The integrated [C II] to ^{12}CO (1 → 0) line ratio is large ($\gtrsim 1000$) in all galaxies studied and is similarly large for Galactic molecular clouds. The [C II] line is therefore energetically very important for the study of giant molecular clouds.

The important new conclusions are as follows:

1. The [C II]/^{12}CO (1 → 0) integrated line intensity ratio is identical for starburst nuclei and OB star formation regions in the Galaxy, indicating that most of the observed CO line intensity from starburst nuclei arises from warm molecular gas exposed to elevated UV fields (> 10^3 times the local interstellar UV radiation field)—not from cold disk clouds. We expect the excitation temperature of CO-emitting gas in these galaxies may be significantly in excess of the 10 K commonly assumed. Therefore, the CO line intensity may trace a *combination of mass and excitation* in starburst nuclei. Consequently the large molecular mass concentrations deduced for starburst nuclei could be partially an excitation effect.

2. For the nonstarburst galaxies in our sample, the [C II]/^{12}CO (1 → 0) line intensity ratio is a factor of 3 smaller than the starburst ratio due to the predominance of non–UV exposed disk molecular clouds. Furthermore, the *brightness* of the [C II] line in the nonstarburst galaxies is similar to the large-scale [C II] measurements in the Milky Way, establishing a *link* between the molecular interstellar medium in our own and other nonstarburst galaxies. This lends support to the growing body of evidence that the interstellar medium in starburst galaxies is quite different from that in our own.

3. Since [C II] line emission is largely associated with OB star formation, the integrated [C II]/^{12}CO (1 → 0) line intensity ratio may be used as a *test of star formation activity*. Comparing these two line intensities with the observed FIR

continuum radiation enables one to place constraints on the intensity and spatial extent of star formation regions in a galaxy. The combination of these three data sets may thus prove to be a good diagnostic tool in determining the spatial extent, and hence, the origins of FIR continuum radiation in ultraluminous galaxies.

4. The measured [C II] line intensity for many of the starburst nuclei accounts for a substantial amount of the observed atomic column density. Therefore, a large fraction of the 21 cm line emission from starburst nuclei may arise in warm dense photodissociation regions—not in more diffuse H I gas, supporting the contention that much of the atomic medium in galaxies may be the result of the photodissociation of molecular clouds by OB stars. Hence, the atomic medium may

in part be the product, not the precursor, of star formation activity.

REFERENCES

Allen, R. J., Atherton, P. D., & Tilanus, R. P. J. 1986, Nature, 319, 296
Beeman, J. W., Haller, E. E., Hansen, W. L., Luke, P. N., & Richards, P. L. 1989, in Proc. of the Third Infrared Technology Workshop, ed. C. Mc-Creight (NASA Technical Memorandum 102209), p. 5
Benvenuti, P., Capaccioli, M., & D'Odorico, S. 1975, A&A, 41, 91
Bloemen, H. 1989, ARA&A, 27, 469
Bosma, A., van der Hulst, J. M., & Sulivan, W. T., II, 1977, A&A, 57, 373
Bottinelli, L., Gouguenheim, L., & Paturel, G. 1980, A&A, 88, 32
Brackman, E., & Scoville, N. Z. 1980, ApJ, 242, 112
Briggs, F. H. 1985, preprint
Burbidge, E. M., & Burbidge, G. R. 1959, ApJ, 129, 271
Burbidge, E. M., Burbidge, G. R., & Pendergast, K. H. 1959, ApJ, 130, 739
Carigan, C. 1985, ApJ, 299, 59
Chokshi, A., Tielens, A. G. G. M., Werner, M. W., & Castelaz, M. W. 1988, ApJ, 334, 803
Cohen, R. S., Dame, T. M., Garay, G., Montani, J., Rubio, M., & Thadeus, P. 1988, ApJ, 331, L95
Cooksy, A. S., Blake, G. A., & Saykally, R. J. 1986, ApJ, 305, L89
Cox, P., & Mezger, P. G. 1987, in Star Formation in Galaxies, ed. C. Persson (Washington, DC: GPO), p. 23
Crawford, M. K., Genzel, R., Townes, C. H., & Watson, D. M. 1985, ApJ, 291, 755 (CGTW)
Crutcher, R. M., Rogstad, D. H., & Chu, K. 1978, ApJ, 255, 784
de Vaucouleurs, G., de Vaucouleurs, A., & Corwin, H. G. 1976, Second Reference Catalog of Bright Galaxies (Austin: University of Texas Press)
Dickel, J. R., Dickel, H. R., & Wilson, W. J. 1978, ApJ, 223, 840
Dickey, J. M. 1982, ApJ, 263, 87
Draine, B. T. 1978, ApJS, 36, 595
Duffy, P. B., Erickson, E. F., Haas, M. R., & Houck, J. R. 1987, ApJ, 315, 68
Dufour, R. J., Shields, G. A., & Talbot, R. J. 1982, ApJ, 252, 461
Eastman, R. G., & Kirshner, R. P. 1989, ApJ, 347, 771
Eckart, A., Downes, D., Genzel, R., Harris, A. I., Jaffe, D. T., & Wild, W. 1990, ApJ, 348, 434
Eckart, A., et al. 1991, in preparation
Ellis, H. B., & Werner, M. W. 1991, in preparation
Emerson, J. P., Furniss, I., & Jennings, R. E. 1975, MNRAS, 172, 411
Fazio, G. G., Kleinmann, D. E., Noyes, R. W., Wright, E. L., Zeilik, M., & Low, F. J. 1974, ApJ, 192, L23
Flaud, J. M., Camy-Peyret, C., & Johns, J. W. C. 1983, Canadian J. Phys., 61, 1462
Frerking, M. A., Langer, W. D., & Wilson, R. W. 1982, ApJ, 262, 590
Gatley, I., Becklin, E. E., Sellgren, K., & Werner, M. W. 1979, ApJ, 233, 575
Gatley, I., Becklin, E. E., Werner, M. W., & Harper, D. A. 1978, ApJ, 220, 822
Gatley, I., Becklin, E. E., Werner, M. W., & Wynn-Williams, C. G. 1977, ApJ, 216, 277
Geis, N., et al. 1991, in preparation
Genzel, R., Harris, A. I., & Stutzki, J. 1989, in Proc. 22nd ESLAB Symposium: Infrared Spectroscopy in Astronomy, ed. B. H. Kaldeich (ESA SP-290), p. 115
Genzel, R., & Stacey, G. J. 1985, Mitt. Astr. Ges., 63, 215
Genzel, R., Stacey, G. J., Harris, A. I., Townes, C. H., Geis, N., Graf, U. U., Poglitsch, A., & Stutzki, J. 1990, ApJ, 356, 160
Genzel, R., Watson, D. M., Crawford, M. K., & Townes, C. H. 1985, ApJ, 297, 766
Gillespie, A. R., Huggins, P. J., Sollner, T. C. L. G., Philips, T. G., Gardner, F. F., & Knowles, S. H. 1977, A&A, 60, 221
Haller, E. E., Hueschen, M. R., & Richards, P. L. 1979, Appl. Phys. Letters, 34, 495
Harper, D. A. 1974, ApJ, 192, 557
Harper, D. A., Low, F. J., Rieke, G. H., & Thronson, H. A. 1976, ApJ, 205, 136
Harris, A. I. 1988, Internat. J. Infrared Millimeter Waves, 9, 231
Harris, A. I., Stutzki, J., Genzel, R., Lugten, J. B., Stacey, G. J., & Jaffe, D. T. 1987, ApJ, 322, L49
Harvey, P. M., Campbell, M. F., & Hoffmann, W. F. 1977, ApJ, 211, 786

Harvey, P. M., Hoffmann, W. F., & Campbell, M. F. 1979, ApJ, 227, 114
Harvey, P. M., Thronson, H. A., Jr., & Gatley, I. 1980, ApJ, 235, 894
Haynes, M. P., Giovanelli, R., & Roberts, M. S. 1979, ApJ, 229, 83
Hollenbach, D., & McKee, C. F. 1989, ApJ, 342, 306
Howe, J. E., Jaffe, D. T., Genzel, R., & Stacey, G. J. 1991, ApJ, 373, 158
Huchtmeier, W. K., Seiradakis, J. H., & Materne, J. 1980, A&A, 91, 341
Hyland, A. R., McGregor, P. J., Robinson, G., Thomas, J. A., Becklin, E. E., Gatley, I., & Werner, M. W. 1980, ApJ, 241, 709
IRAS Point Source Catalog. 1985, Joint IRAS Science Working Group (Washington, DC: GPO)
Irwin, J. A., Seaquist, E. R., Taylor, A. R., & Duric, N. 1987, ApJ, 313, L91
Jaffe, D. T., Genzel, R., Harris, A. I., Howe, J. E., Stacey, G. J., & Stutzki, J. 1990, ApJ, 353, 265
Johns, J. W. C. 1985, J. Opt. Soc. America B 2, 1340
Joy, M., Lester, D. F., Harvey, P. M., & Ellis, H. B., Jr. 1988, ApJ, 326, 662
Joy, M., Lester, D. F., Harvey, P. M., Telesco, C. M., Decher, R., Rickard, L. J, & Bushouse, H. 1989, ApJ, 339, 100
Jura, M. 1978, in Protostars and Protoplanets, ed. T. Gehrels (Tucson: University of Arizona Press), p. 165
Kulkarni, S. R., & Heiles, C. H. 1988, in Galactic and Extragalactic Radio Astronomy, ed. K. I. Kellermann and G. L. Verschuur (Berlin: Springer), p. 95
Kurtz, N. T., Smyers, S. D., Russell, R. W., Harwit, M., & Melnick, G. 1983, ApJ, 264, 538
Kutner, M. L., & Leung, C. M. 1985, ApJ, 291, 188
Kutner, M. L., Machik, D. E., Mead, K. N., & Evans, N. J., II 1985, ApJ, 299, 351
Lada, C. J., Thronson, H. A., Jr., Smith, H. A., Harper, D. A., Keene, J., Loewenstein, R. F., & Smith, J. 1981, ApJ, 251, L91
Langer, W. 1976, ApJ, 206, 699
Liszt, H. S., Burton, W. B., & van der Hulst, J. M. 1985, A&A, 142, 237
Liszt, H. S., van der Hulst, J. M., Burton, W. B., & Ondrechen, M. P. 1983, A&A, 126, 341
Lo, K. Y., Cheung, K. W., Masson, C. R., Phillips, T. G., Scott, S. L., & Woody, D. P. 1987, ApJ, 312, 574
Lord, S. D., et al. 1991, in preparation
Loren, R. B., Plambeck, R. L., Davis, J. H., & Snell, R. L. 1981, ApJ, 245, 495
Low, F. J., & Aumann, H. H. 1970, ApJ, 162, L79
Lugten, J. B. 1987, Ph.D. thesis, University of California, Berkeley
Lugten, J. B., Genzel, R., Crawford, M. K., & Townes, C. H. 1986a, ApJ, 306, 691
Lugten, J. B., Watson, D. M., Crawford, M. K., & Genzel, R. 1986b, ApJ, 311, L51
Maloney, P., & Black, J. H. 1988, ApJ, 325, 389
Makinen, P., Harvey, P. M., Wilking, B. A., & Evans, N. J. 1985, ApJ, 299, 341
Matsuhara, H., et al. 1989, ApJ, 339, L67
McCall, M. L. 1989, AJ, 97, 1341
Melnick, G., Stacey, G. J., Viscuso, P. J., & Fuller, C. E. 1986, ApJ, 303, 638
Milman, A. S., Knapp, G. R., Kerr, F. S., Knapp, S. L., & Wilson, W. J. 1975, AJ, 80, 93
Moseley, H. 1980, ApJ, 238, 892
Mufson, S. L., & Liszt, H. S. 1977, ApJ, 212, 664
———. 1979, ApJ, 232, 451
Mufson, S. L., Lyon, J., & Marionni, P. A. 1975, ApJ, 201, L85
Newton, K. 1980, MNRAS, 191, 615
Nilson, P. 1973, Uppsala General Catalogue of Galaxies (Uppsala: Uppsala Astronomical Observatory)
Okuda, H., et al. 1989, in IAU Symposium 136, The Center of the Galaxy, ed. M. Morris (Dordrecht: Kluwer), p. 145
Olofsson, H., & Rydbeck, G. 1984, A&A, 136, 17
Poglitsch, A., et al. 1991a, in preparation
Poglitsch, A., et al. 1991b, in preparation
Rengarajan, T. N., Cheung, L. H., Fazio, G. G., Shivanadan, K., & McBreen, B. 1984, ApJ, 286, 573

Rice, W., Lonsdale, C. J., Soifer, B. T., Neugebauer, G., Koplan, E. L., Lloyd, L. A., deJong, T., & Habing, H. J. 1988, ApJS, 68, 91
Richmond, M. W., & Knapp, G. R. 1986, AJ, 91, 517
Rickard, L. J, & Blitz, L. 1985, ApJ, 292, L57
Rickard, L. J, & Harvey, P. M. 1984, AJ, 89, 152
Rieke, G. H., Cutri, R. M., Black, J. H., Kailey, W. F., McAlary, C. W., Lebofsky, M. J., & Elston, R. 1985, ApJ, 290, 116
Rieke, G. H., Lebofsky, M. J., Thompson, R. I., Low, F. J., & Tokunaga, A. T. 1980, ApJ, 238, 24
Rodriguez Espinosa, J. M., Rudy, R. J., & Jones, B. 1986, ApJ, 309, 76
Rogstad, D. H., Lockhart, I. A., & Wright, M. C. H. 1974, ApJ, 193, 309
Rohlfs, K., Kreitschmann, J., Siegman, B. C., & Feitzinger, J. V. 1984, AJ, 137, 343
Rowan-Robinson, M., Phillips, T. G., & White, G. 1980, A&A, 82, 381
Russell, R. W., Melnick, G. J., Gull, G. E., & Harwit, M. 1980, ApJ, 240, L99
Russell, R. W., Melnick, G. J., Smyers, S. D., Kurtz, N. T., Gosnell, T. R., Harwit, M., & Werner, M. W. 1981, ApJ, 250, L35
Sancisi, R., & Allen, R. J. 1979, A&A, 74, 73
Sandage, A., & Tammann, G. A. 1975, ApJ, 196, 313
———. 1981, A Revised Shapley-Ames Catalogue of Bright Galaxies (Washington, DC: Carnegie Institution of Washington)
Sanders, D. B., Clemens, D. P., Scoville, N. Z., & Solomon, P. M. 1986, ApJS, 60, 1
Sanders, D. B., & Mirabell, I. F. 1985, ApJ, 298, L31
Sargent, A. I., Sutton, E. C., Masson, C. R., Lo, K. Y., & Phillips, T. G. 1985, ApJ, 289, 150
Schloerb, F. P., & Loren, R. B. 1982, in Symposium on the Orion Nebula to Honor Henry Draper, Ann. NY Acad. Sci., 395, 32
Schmid-Burgk, J., et al. 1989, A&A, 215, 150
Scoville, N. Z., & Young, J. S. 1983, ApJ, 265, 148
Serabyn, E., & Güsten, R. 1987, A&A, 184, 133
Shane, W. W. 1975, in La Dynamique des Galaxies Spirales, ed. L. Weliachew (Paris: CNRS), p. 217
Shibai, H., et al. 1991, ApJ, in press
Smith, J. 1982, ApJ, 261, 463
Solomon, P. M., & Sage, L. J. 1988, ApJ, 334, 613
Spinrad, H., Bahcall, J., Becklin, E. E., Gunn, J. E., Kristian, J., Neugebauer, G., Sargent, W. L. W., & Smith, H. 1973, ApJ, 180, 351
Stacey, G. J. 1985, Ph.D. thesis, Cornell University
Stacey, G. J., Viscuso, P. J., Fuller, C. E., & Kurtz, N. T. 1985, ApJ, 289, 803
Stacey, G. J., et al. 1991, in preparation
Sternberg, A. 1988, ApJ, 332, 400
Sternberg, A., & Dalgarno, A. 1989, ApJ, 338, 197

Storey, J. W. V., Watson, D. M., & Townes, C. H. 1980, Internat. J. Infrared Millimeter Waves, 1, 15
Storey, J. W. V., et al. 1991a, in preparation
Storey, J. W. V., et al. 1991b, in preparation
Stutzki, J., Stacey, G. J., Genzel, R., Harris, A. I., Jaffe, D. T., & Lugten, J. B. 1988, ApJ, 332, 379
Tacconi, L. J., & Young, J. S. 1986, ApJ, 308, 600
Telesco, C. M., & Harper, D. A. 1977, ApJ, 211, 475
———. 1980, ApJ, 235, 392
Thronson, H. A., Jr., & Harper, D. A. 1979, ApJ, 230, 133
Thronson, H. A., Jr., & Lada, C. J. 1983, ApJ, 269, 175
Thronson, H. A., Jr., Lada, C. J., Schwartz, P. R., Smith, H. A., Smith, J., Glaccum, W., Harper, D. A., & Loewenstein, R. F. 1984, ApJ, 280, 154
Tielens, A. G. G. M., & Hollenbach, D. 1985, ApJ, 291, 722
Tilanus, R. P. J., & Allen, R. J. 1989, ApJ, 339, L57
Tucker, K., Kutner, M., & Thaddeus, P. 1973, ApJ, 186, L13
Ulich, B. L., & Haas, R. W. 1976, ApJS, 30, 247
van der Hulst, J. M., Golisch, W. F., & Haschick, A. D. 1983, ApJ, 264, L37
Vogel, S. N., Kulkarni, S. R., & Scoville, N. Z. 1988, Nature, 334, 402
Walmsey, M. 1975, in H II Regions and Related Topics, ed. T. Wilson & D. Downes (New York: Springer), p. 17
Watson, D. M. 1982, Ph.D. thesis, University of California, Berkeley
Watson, D. M., Genzel, R., Townes, C. H., Werner, M. W., & Storey, J. W. V. 1984, ApJ, 279, L1
Watt, G. D., Burton, W. B., Choe, S.-U., & Liszt, H. S. 1986, A&A, 163, 194
Werner, M. W. 1970, Ap. Letters, 6, 81
Werner, M. W., Becklin, E. E., Gatley, I., Ellis, M. J., Hyland, A. R., Robinson, G., & Thomas, J. A. 1978, MNRAS, 184, 365
Werner, M. W., et al. 1980, ApJ, 242, 601
Werner, M. W., Gatley, I., Harper, D. A., Becklin, E. E., Loewenstein, R., Telesco, C. M., & Thronson, H. A., Jr. 1976, ApJ, 204, 420
Whitcomb, S. E., Gatley, I., Hildebrand, R. H., Keene, J., Sellgren, K., & Werner, M. W. 1981, ApJ, 246, 416
Wild, W., et al. 1991, in preparation
Wilson, T. L., Fazio, G. G., Jaffe, D. T., Kleinmann, D. E., Wright, E. L., & Low, F. J. 1979, A&A, 76, 86
Wolfire, M. G. L., Hollenbach, D., & Tielens, A. G. M. 1989, ApJ, 344, 770
Wright, M. C. H., & Seielstad, G. A. 1973, Ap. Letters, 13, 1
Young, J. S., Claussen, M. J., Kleinmann, S. G., Rubin, V. C., & Scoville, N. Z. 1988, ApJ, 331, L81
Young, J. S., & Sanders, D. B. 1986, ApJ, 302, 680
Young, J. S., & Scoville, N. Z. 1984, ApJ, 287, 153
Young, J. S., Tacconi, L. J., & Scoville, N. Z. 1983, ApJ, 269, 136